Journal of *Marine Science and Engineering*

MDPI

Article

Fine Particle Migration in a Gas Hydrate Sand: Single- and Two-Phase Fluid Using a Device for Observation at the Pore Scale

Jie He [1,2,3], Xiang Huang [1,2,4,*] and Pei Cao [3,5]

[1] College of Civil Engineering, Tongji University, Shanghai 200092, China; hejie@tongji.edu.cn
[2] State Key Laboratory for Disaster Reduction in Civil Engineering, Tongji University, Shanghai 200092, China
[3] Key Laboratory of Geotechnical and Underground Engineering of Ministry of Education, Tongji University, Shanghai 200092, China; pcao@tongji.edu.cn
[4] College of Civil Engineering, Guangxi Polytechnic of Construction, Nanning 530007, China
[5] Department of Geotechnical Engineering, Tongji University, Shanghai 200092, China
* Correspondence: huangx@alumni.tongji.edu.cn

Abstract: The production of natural gas hydrates will change the cementation strength, porosity, and effective stress in the stratum, which may lead to engineering and geological disasters. Sand production is a phenomenon where sand particles are carried out of the reservoir along with fluids during gas extraction, posing challenges to safe and sustainable production. This study explored the mechanism of fine particle migration in multiphase flow by a microscopic visualization test device. The device can inject a gas–liquid–solid phase at the same time and allow real-time observation. Experimental tests on fine particle migration of single- and two-phase fluid flow were carried out considering different conditions, i.e., fine particle concentration, fine particle size, fluid flow rate, and gas–liquid ratio. The results show that in single-phase fluid flow, the original gas will gradually dissolve in the liquid phase, and finally stay in the test device as bubbles, which can change the pore structures, resulting in the accumulation of fine particles at the gas–liquid interface. In two-phase fluid flow with mixed gas–water fluids, there are two flow modes of gas–liquid flow: mixed flow and separated flow. The interfacial tension at the gas–liquid interface can effectively migrate fine particles when the gas–liquid flows alternately and the sand production rate further increases as the gas–liquid ratio increases. In addition, changes in the concentration of fine particles, particle size, fluid flow rate, and the gas–liquid ratio will affect the migration of fine particles, leading to differences in the final sand production.

Keywords: sand production; multi-phase flow; interfacial tension; microscopic visualization

Citation: He, J.; Huang, X.; Cao, P. Fine Particle Migration in a Gas Hydrate Sand: Single- and Two-Phase Fluid Using a Device for Observation at the Pore Scale. *J. Mar. Sci. Eng.* **2024**, *12*, 109. https://doi.org/10.3390/jmse12010109

Academic Editor: Dmitry A. Ruban

Received: 12 December 2023
Revised: 1 January 2024
Accepted: 3 January 2024
Published: 6 January 2024

1. Introduction

Seeking alternative green and clean energy has become a major national development demand in many countries. Sequestering twice the total carbon content of conventional fossil energy [1], natural gas hydrates are regarded as a promising alternative energy resource in the post-oil era. Natural gas hydrates are widespread, particularly in voids of marine sediments forming unconsolidated reservoirs of hydrates [2], where a natural gas supply is adequate, and pressure and temperature are appropriate for stable hydrates. Presently, the major production approaches involve depressurization, heating (thermal stimulation), chemical inhibition injection, CO_2 swapping, and their combinations [3,4]. Nevertheless, as methane recovery approaches the commercial demonstration stage of development, concerns about undesirable mechanical responses may arise, such as the reformation of hydrate near wellbores, the rise in bottom well pressure, geomechanical effects, seafloor subsidence, submarine landslides, and sand production [4,5].

Sand production is a phenomenon where sand particles are carried out of the reservoir along with fluids during gas extraction. As production-induced hydrate dissociation causes

de-cementation and enlargement of voids in the matrix of reservoirs, fine particles become mobile and likely migrate with fluids towards the wells under a high-pressure drop, causing damage/malfunction in the wells and production shutdown. The destructive impact of sand production is reported in trial production implemented in the Nankai Trough of Japan [6–11] in addition to other inland hydrate reservoirs [12–15]. Therefore, effective sand control is vital for achieving sustainable long-term operation, while understanding the fundamental behavior of fines that migrate through pore networks is a prerequisite.

Field tests of sand production are practically prohibitive due to extremely high costs and labor. Therefore, research on sand production is mainly based on numerical simulations and laboratory experimental methods.

Sand production is a multi-field (thermo-hydro-mechanical, THM)-coupled multi-phase (solid–liquid–gas) flow process accompanied by a complex phase transition [16]. Uchida et al. (2016) introduced a THM-coupled model along with a sand migration model, their model quantitatively forecasted sand production by assuming equal superficial velocities for solids and fluids [17]. Ning et al. (2017) developed a model for sand production by employing one-way coupling and they indicated that, during short-term production, reservoir stability is not a significant issue; instead, the primary challenge lies in balancing sand production control with ensuring gas production [18]. In addition, several numerical models for sand production prediction have been proposed [19,20]. However, establishing the critical conditions for sand production remains challenging and the effects of a depressurization strategy and sand control criterion on sand, gas, and water production need further study.

Furthermore, laboratory experiments are carried out under different conditions, such as occurrence environments, mining methods, pore sizes, particle sizes, and hydraulic conditions. Oyama et al. (2010) experimentally modeled sand production during an unstable depressurization process and found that the water flow rate is the key factor of sand production onset [21]. Jung et al. (2012) investigated the role of fine particles on gas production and it was found that even if the content of fine particles is relatively low, it is also important for the migration and blockage of fine silt particles in the gas produced by hydrate-bearing sediments [22]. Murphy et al. (2020) designed an apparatus to simulate a plane strain case of sand production based on the production trial in Nankai Trough, Japan in 2013 [23]. It was found that the initiation mechanism of sand production is related to the flow rate and excess pore pressure. Lu et al. (2018) found that sand production is related to sand content, particle size, and gas production rate based on experiments [24]. Okwananke et al. (2019) experimentally explored the migration of fluid at different gas hydrate-bearing sediments by measuring gas permeability, finding that it is dominated by capillary breakthrough, pore/grain size distribution, hydrate clogging, hydrate-forced heave or agglomeration, and Klinkenberg effect [25].

The above-mentioned test devices study the sand production of hydrates from a macroscopic perspective. The limitation of such experimental devices is that they make it hard to observe the migration of gas, water, and solid particles in the hydrate pores during the hydrate decomposition process in real time, which is not conducive to an in-depth understanding of the sand production mechanism. Some scholars tried to study the changes and movement of the three-phase substances in hydrate sediments by using microscopic imaging methods such as CT scanning and X-ray. Li et al. (2019) scanned the formation process of the hydrate by X-ray tomography, and the permeability of hydrate sediments was affected by the microstructure [26]. Hu et al. (2020) investigated the pore structure and spatial distribution of pore materials in hydrate-bearing sediments using a CT scanning technique [27]. Since hydrate sand production involves complex phase changes and the change process is relatively fast, it is difficult to observe hydrate sand production in real time by the current mainstream 3D imaging method of microscopic pore structure. Therefore, some scholars are focusing on two-dimensional microstructure imaging technology. Zhang et al. (2010) developed a microfluidic pore structure etched into a silicon wafer as a 2D model subsurface sedimentary system to investigate the influence of calcium

carbonate mineral precipitation on formation permeability, groundwater remediation, and geological carbon sequestration by injecting $CaCl_2$ and Na_2CO_3 into the micro model [28]. Jung et al. (2018) investigated the migration of fine particles and bridging behavior in a structure mimicking porous media using microfluidic pore models [29]. Song et al. (2018) conducted a series of microscopic CO_2 flooding experiments under high temperatures and high confining pressures and observed the dynamics of precipitation and deposition in the pores from a 2D micromodel [30]. Cao et al. (2019) conducted 2D micromodel experiments with different pore-throat widths to study the blockage of fine particles and showed that clogging depended on the ratio of particle-to-pore throat size or formed due to bridging or blocking by clusters of the smaller particles [31]. However, the above 2D test devices cannot inject gas–solid–liquid phases at the same time and are unable to restart the actual flow, making it is hard to investigate the mechanism of fine particle migration in multiphase flow.

In this study, a 2D micromodel model device is developed for fine-grain migration that simulates the mining conditions to study the solid–liquid flow and gas–solid–liquid flow migration mechanism and microscopic dynamic sand production variation. First, the microscopic visualized sand production test equipment is introduced. Then, the experimental process is elaborated in detail. By changing the fine particle concentration, fine particle size, fluid flow rate, and gas–liquid ratio, the developed test device is used to simulate the solid–liquid flow and gas–solid–liquid flow. The variation in fine grain migration and macro- and meso-dynamic sand production is analyzed by combining the test results of single-phase fluid flow and two-phase fluid flow.

2. Materials and Methods

2.1. Testing Apparatus

The whole device is divided into two rectangular parallelepiped cabinets, as shown in Figure 1a. The left cabinet is equipped with a microscopic percolation chip module (Suzhou Wenhao Chip Technology Co., Ltd., Suzhou, China), high- and low-temperature control components (Jiangsu Kedi Scientific Research Instrument Co., Ltd., Nantong, China), microscope (Olympus (China) Co., Ltd., Beijing, China), and injection components, including an injection pump, confining pressure pump, and back pressure pump (Jiangsu Kedi Scientific Research Instrument Co., Ltd., Nantong, China). The microscope used is an Olympus SZ61 Stereo Microscope, which is equipped with a zoom ratio of 6.7:1 and provides a magnification range from 6.7× to 45× with a 10× eyepiece.

The cabinet on the right side is installed with the general control of the device, gas flow controller (Beijing SEVENSTAR Electronic Technology Co. Ltd., Beijing, China), computer, and outlet metering components (Jiangsu Kedi Scientific Research Instrument Co., Ltd., Nantong, China), including a gas–solid–liquid separator, gas–liquid separator, dryer, gas flow meter, and electronic balance. The whole device is about 1.5 m in length, 0.5 m wide, and 1.8 m high. The stirring piston vessel, as shown in Figure 1b, is made of 304 stainless steel with an effective volume of 200 mL and pressure resistance of 5 MPa. It is used to store a certain amount of water and fine particles in advance. The stirring piston container is placed on the magnetic suction base, and the bottom of the container is equipped with a magnetic stirrer, which is ellipsoidal, 30 mm long, and 8 mm high, as shown in Figure 1b. The rotational frequency is about 200 rpm, and through the rotation of the rotor, the solution in the container is stirred evenly. The evenly stirred solution is injected through the injection pump according to the set flow or pressure, and the container keeps stirring during injection to maintain a uniform state of mixing. The injected solution and the gas with a given flow ratio are mixed evenly in the pipeline and then injected into the microscopic percolation chip. As shown in Figure 1c, the gas–solid–liquid separator is used to separate fine particles to achieve sand production measurement by a filter net. The gas–liquid separator is used to separate liquid and gas and achieve the measurement of liquid using a balance. The balance adopted is the Huachao Hi-Tech brand high-precision electronic balance with a range of 500 g and an accuracy of 0.001 g. The balance data

can be transmitted to the computer in real time. A gas flow meter is used to measure the outlet gas quantity with a range of 0–50 mL/min and pressure resistance of 3 MPa. It can record instantaneous flow and cumulative flow. A stereo microscope is used to observe the movement of gas, solid, and liquid in the two-dimensional microscopic percolation chip. It can interface with the computer to save the collected images for analysis.

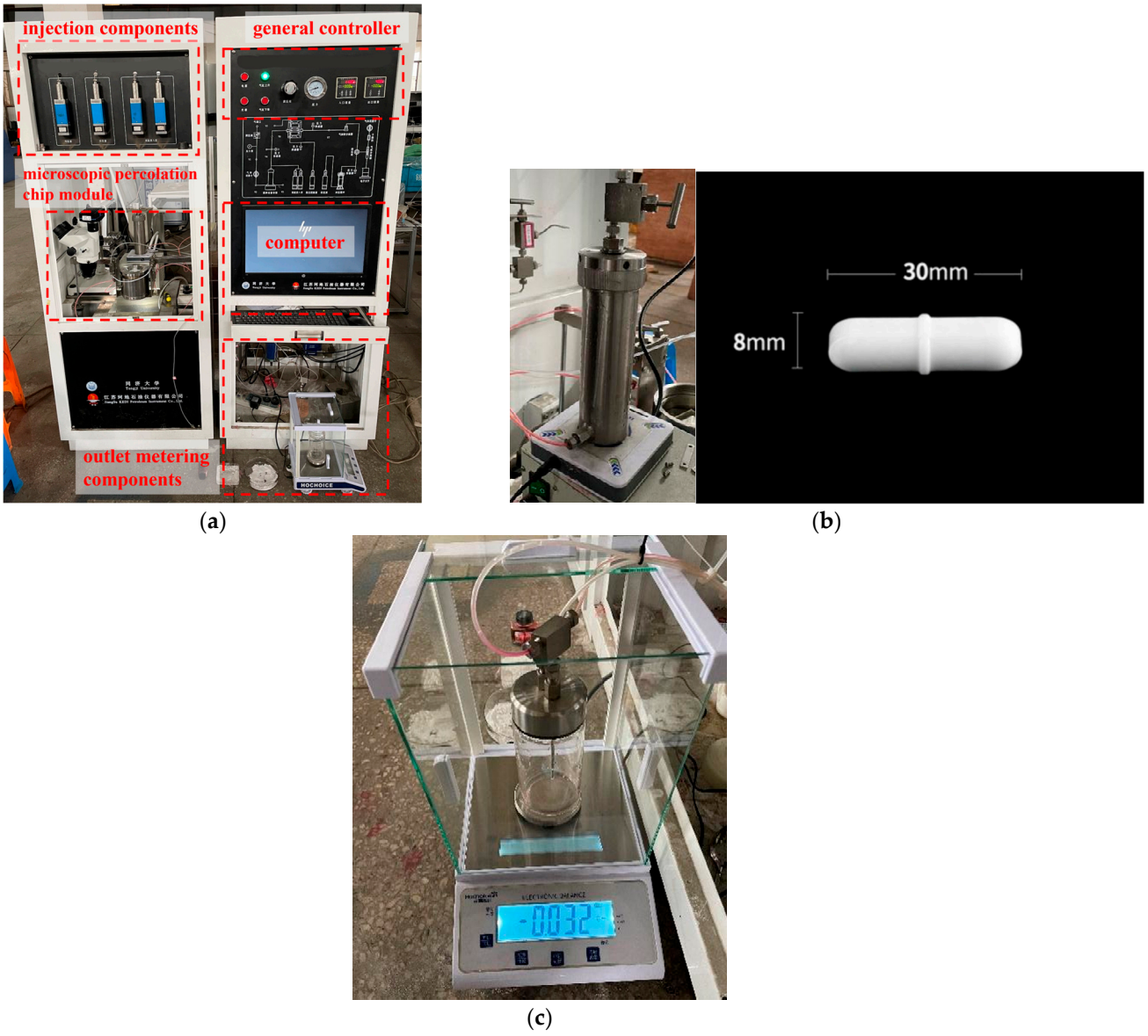

Figure 1. Photos of the apparatus. (**a**) Device physical photos; (**b**) stirred piston vessel and magnetic stirrer; (**c**) solid–liquid separator and electronic balance for liquid weighing.

The 2D microscopic percolation chip module is composed of a pressure protection chamber, a 2D microscopic percolation chip, and high- and low-temperature control components. As shown in Figure 2, the pressure protection chamber is a cylinder made of stainless steel. The cylinder has an outer diameter of 130 mm, an inner diameter of 110 mm, and a height of 121 mm. The interior of the cylinder is a sealed chamber in which a glass carrier platform is arranged to hold the microscopic percolation chips. The size of the glass carrier is matched to that of the microscopic percolation chip. The microscopic percolation chip can be fixed on the glass-carrying platform by pressing the plate and screw, and the glass-carrying platform is provided with a fluorine sealant ring to ensure that the fluid flows through the microporous chip without other free seepage channels. The top and bottom of the pressure protection chamber are equipped with transparent pressure-resistant glass as

observation windows to realize real-time observation of the seepage process. The upper cover of the pressure protection chamber is detachable to facilitate the disassembly and replacement of the microscopic percolation chip. The pressure protection chamber is provided with a microscopic percolation chip inlet and outlet, a confining pressure inlet, and a confining pressure exhaust port, which are used for injecting fluid into the microscopic percolation chip and applying confining pressure to the protection chamber.

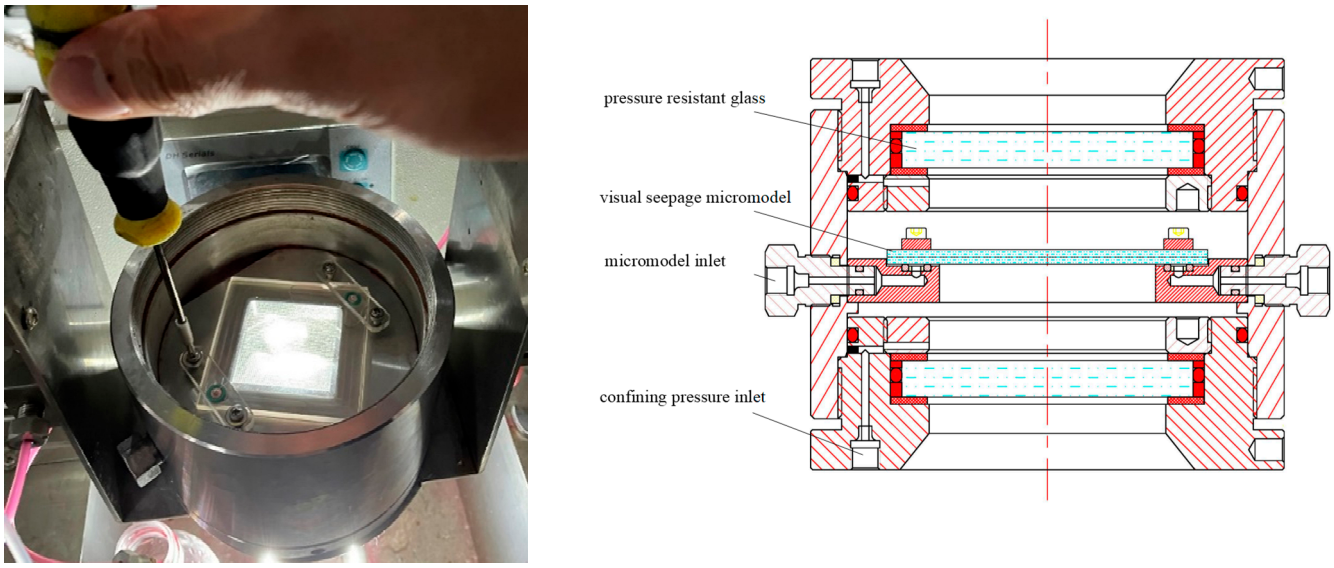

(**a**) (**b**)

Figure 2. Schematic diagram of the pressure protection chamber. (**a**) Physical photos; (**b**) schematic diagram.

Figure 3 shows the 2D microscopic percolation chip used in the device, which is prepared by hydrofluoric acid etching glass technology, and has transparent and corrosion-resistant properties. The microscopic percolation chip is 63.5 mm in length and width, with an overall thickness of 4 mm, and is made of two pieces of glass with a thickness of 2 mm. There are seepage channels between the pieces of glass. The seepage area is 40 mm × 40 mm. The inlet and outlet holes are located on the diagonal of the chip to obtain a longer seepage path. Due to this characteristic, the fluid mainly flows along the diagonal after entering the chip, with less flow occurring in the corner regions. So, we roughly divided the chip into the main flow area and the corner flow area by connecting the midpoint of each side along the diagonal flow line. A large number of regular cylinders are etched in the chip seepage channel to simulate large-particle deposits that are not easily transported in the pore structure of the reservoir. The design of cylinders is based on previous studies on the transport and plugging of fine sand and the distribution of fine particle grain sizes in the gas hydrate reservoir of the South China Sea. As shown in Figure 4, Bigna et al. (1994) [32], Oyeneyin et al. (1995) [33], and Khilar and Fogler (1998) [34] investigated the relationship between host particle size (D), fine particle size (d), pore throat size (o), and clogging behaviors. At present, the hydrate reservoirs discovered in China are all clayey silt reservoirs with an average particle size ranging from 10 to 60 μm [35]. Based on the above factors, we designed the porous media configuration: the pore size of the chip is 500 μm in diameter, 350 μm in spacing, and 150 μm in seepage channel height. The lower seepage channel height is adopted to avoid the influence of the vertical flow, approximately simulating the pore flow in a 2D plane.

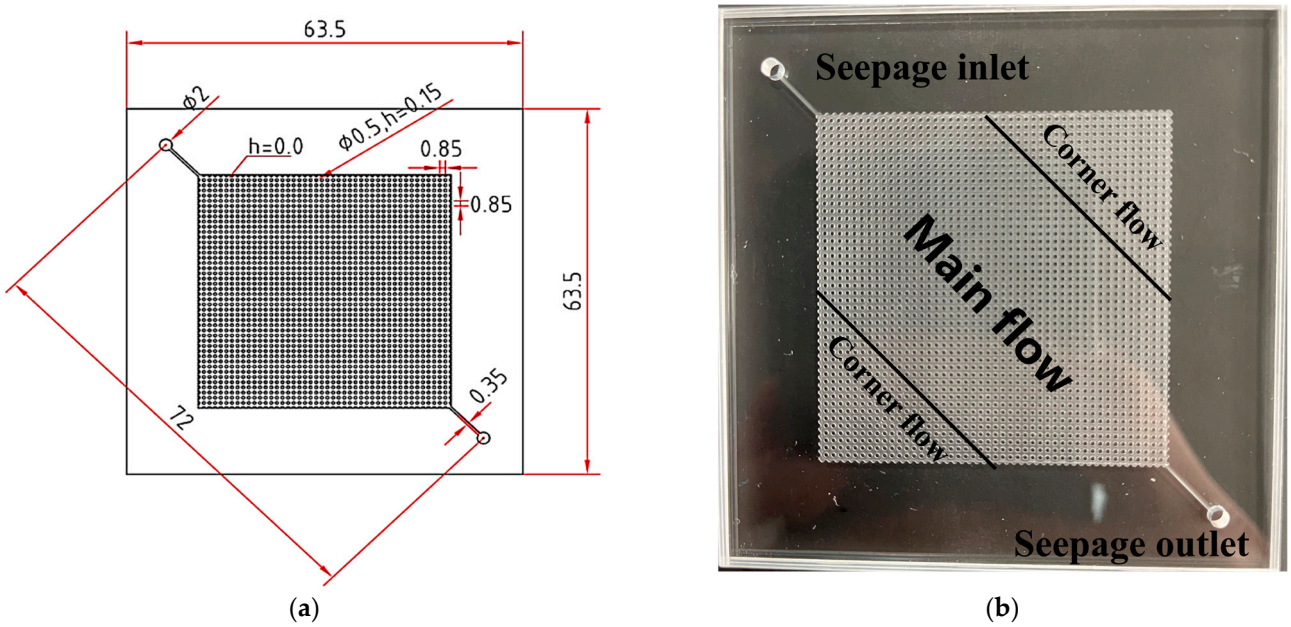

Figure 3. Physical image of the two-dimensional microscopic percolation chip. (**a**) Schematic diagram; (**b**) physical photos.

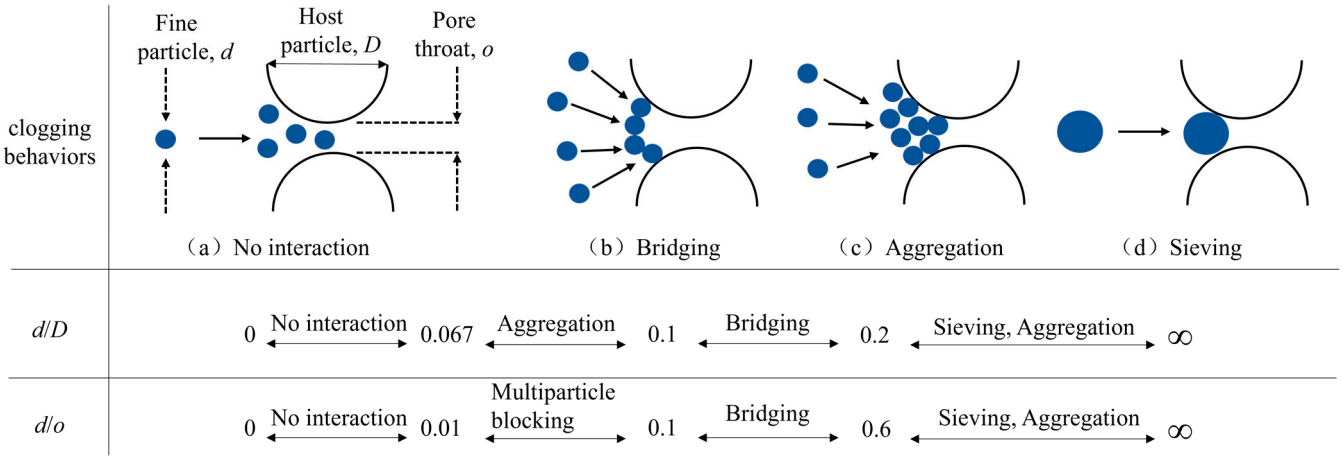

Figure 4. Relationship between host particle size (*D*), fine particle size (*d*), pore throat size (*o*), and clogging behaviors.

2.2. Experimental Setup

2.2.1. Procedure

The overall process of the visualized microscopic test of fine particle migration is as follows:

Step I: Pre-experiment: Initial state setting

(1) Initially, the outlet of the piston container is sealed, and 150 mL of liquid is carefully poured using a beaker. (2) Subsequently, the necessary mass of fine particles is meticulously calculated based on the mass concentration and then added to the container after being weighed with precision. (3) Following this, 1 mL of red ink is measured using a dropper and gently introduced into the container as a liquid chromogenic agent. (4) Placing the container onto the stirring base, it is stirred for thirty seconds to ensure an even mixture of the solution (the stirring time can be adjusted according to the actual situation). (5) Turning the container upside down, the connecting rod is used to push the piston into the container, effectively expelling any trapped air. (6) The container is then filled with water, (7) and the lid is securely fastened, assembling the stirring piston container. (8) Finally, the inlet of the

stirring piston container is connected to the injection pump, while the outlet is linked to the injection pipe, initiating stirring on the rotating base.

Step II: Experiment

The experiment is carried out under the condition of normal temperature and pressure. As it is difficult to achieve high pressures in indoor experiments, we consider the effects of high pressure in compressing pore spaces and altering pore structure. Hence, we simulated pore flow under high-pressure conditions by using smaller pore spacings and characterized the flow situation through pressure differentials.

Furthermore, as methane gas is flammable, explosive, and extremely insoluble in water, it costs a lot to achieve the temperature and pressure conditions required for solubility in the reservoir. For the sake of laboratory safety and accurate control of the gas–liquid ratio, CO_2 is used instead of methane. Methane and CO_2 behave very differently with water under room temperature and pressure; in particular, their solubility varies greatly, and methane is much less soluble in water. However, under low temperatures and high pressure in the reservoir, the solubility of methane increases significantly, approaching that of CO_2 at room temperature and pressure. Therefore, it is reasonable to investigate fine particle migration with CO_2 instead of methane.

After the initial state setting, the chip outlet valve is opened, and the suspension is injected into the microscopic percolation chip; the microscope is operated to observe the flow in different areas during the test, informed by real-time curve test current status.

The valve at the outlet end of the chip is open to pass the fine particle suspension into the chip according to the experimental conditions. During the test, the microscope window was adjusted to observe the flow in different areas. After a total of 50 mL, fine particle suspension is passed through, and the chip outlet valve is closed to flush out the residual fine particle suspension in the pipeline at the back end of the chip. Then, the collected solid–liquid suspension is dried and weighed.

Step III: Post experiment: Experimental Closeout

When the test is finished, the liquid pumps and gas flow controllers are first stopped, and the outlet valve of the micro-percolation chip and the valve between the injection pump and the stirring piston container are closed. The valve between the injection pump and the chip of the outlet ends is opened. The residual fine particle suspension in the pipe from the chip outlet end to the solid–liquid collector is driven out with clear water. When the outflowing liquid is clear water, the injection can be stopped. After saving the test data, the collected solid–liquid mixture is dried in a blast drying oven, in which the drying temperature is 160 °C, and the drying time is 2 h. After drying, the solid–liquid collector is weighed, cleaned, and then dried and weighed again. The difference between the two weights is the mass of the discharged fine particles. Due to the fine particles very easily causing chip and pipeline blockage, the equipment should be cleaned in time after the test.

2.2.2. Testing Program

Four group tests, i.e., groups I–IV shown in Table 1, were carried out to study the fine particle migration under single-phase fluid flow, considering the effects of different particle sizes, fine particle concentrations, and flow rates on fine particle migration. The main components of fine particles in the non-diagenetic reservoirs in the South China Sea are quartz, illite, montmorillonite, etc., among which quartz content is the highest [36]. Therefore, silica sand was selected for testing. The fine particles used in the experiment were obtained by grinding and sieving silica sand from the Donghai area of Jiangsu Province. The shape is vein-like, plate-like, lenticular, cystic, irregular, etc. And the region's silica sand metallogenic environment is affected by subduction metamorphism fluid dehydration and mixed with meteoric factors. Three types of fine particles of silica sand were selected for the test, each of which is 300-mesh (48 μm), 600-mesh (23 μm), and 1000-mesh (13 μm). Basic groups were set up in each large group to facilitate a comparative analysis of results within and across groups. Fine particles in group 5, shown in Table 1, were selected at a fine particle concentration of 3% with 300-mesh size for an in-depth study of the variation

in fine particle migration under two-phase fluid flow. The gas–liquid ratio is changed by controlling the injection rate of the gas–liquid two-phase, considering the influence of 3 different water–gas ratios on the migration of fine particles, and repeating each under the same conditions.

Table 1. Experimental groups for the transport of fine particles.

	Group	Fine Particle Size (mesh)	Fine Particle Concentration (%)	Solid Load (mg/min)	Liquid Flow Rate (mL/min)	Gas Flow Rate (mL/min)	Gas–Liquid Ratio	Test Purposes
I	Basic group 1	300	3	24	0.8	/	/	Influence of different concentrations
	1.1	300	1	8	0.8	/	/	
	1.2	300	5	40	0.8	/	/	
	1.3	300	10	80	0.8	/	/	
II	Basic group 2	300	3	24	0.8	/	/	Influence of different flow rates
	2.1	300	3	24	0.4	/	/	
	2.2	300	3	24	1.2	/	/	
	2.3	300	3	24	1.6	/	/	
III	Basic group 3	600	3	24	0.8	/	/	The migration variation of 600-mesh fine particles under different concentrations
	3.1	600	1	8	0.8	/	/	
	3.2	600	5	40	0.8	/	/	
	3.3	600	10	80	0.8	/	/	
IV	Basic group 4	1000	3	24	0.8	/	/	The migration variation of 1000-mesh fine particles under different concentrations
	4.1	1000	1	8	0.8	/	/	
	4.2	1000	5	40	0.8	/	/	
	4.3	1000	10	80	0.8	/	/	
V	5.1	300	3	24	0.6	0.2	1:3	fine particle migration of two-phase fluid flow
	5.2	300	3	24	0.6	0.2	1:3	
	5.3	300	3	24	0.4	0.4	1:1	
	5.4	300	3	24	0.4	0.4	1:1	
	5.5	300	3	24	0.2	0.6	3:1	
	5.6	300	3	24	0.2	0.6	3:1	

2.2.3. Calibration

It is necessary to calibrate the concentration of the solution discharged from the stirring piston vessel to check whether the stirring piston vessel is effective and whether the fine particles are evenly dispersed. During calibration, the configured suspension was injected into the stirring piston vessel following the aforementioned method, and the injection pump was set to inject 50 mL of liquid at the same flow rate. Under the condition that the stirring piston vessel kept stirring, the discharged fine particle suspension was directly collected, dried, and weighed, the discharged fine particle mass was counted, and the solution concentration was calculated. For fine particles with a particle size of 300 mesh (48 μm), 600 mesh (23 μm), and 1000 mesh (13 μm), two repeatability calibration tests with suspension concentrations of 1%, 3%, 5%, and 10% were conducted to obtain the fine particles with the corresponding size by using a customized standard sample screen. The results are combined and plotted in Figure 5.

The concentration of fine particles in the solution obtained from the calibration test is lower than the theoretical concentration, which should be related to the structure of the stirring piston container itself. In the process of discharging the solution, the fine particles in the container cannot be evenly discharged due to the stirring, resulting in a low concentration. The concentrations of the solutions with particle sizes of 600 mesh and 1000 mesh are relatively close, while the concentration of fine particles with 300-mesh size is significantly lower than that of 600-mesh and 1000-mesh particles. The calibrated concentration results of the three particle sizes can be linearly fitted with a straight line, indicating that, although the concentration of fine particles in the outflow solution in the stirring piston container is low, the concentration of the solution is relatively stable.

Changing the mass of fine particles added to the solution will change the concentration of fine particles accordingly. The subsequent relevant calculations can be based on the results of the concentration calibration curve.

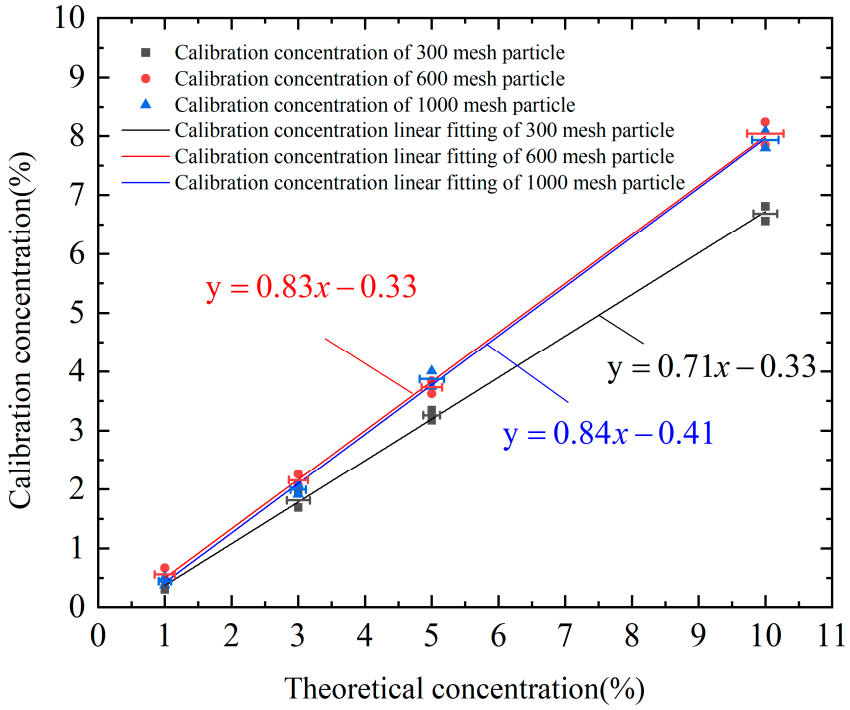

Figure 5. Fitting lines of the calibration test results of the stirring piston container.

3. Results

3.1. Fines Migration with Gas-Free Flow

3.1.1. Sanding Process

The sand production rate is introduced:

$$n_{SPR} = \frac{m_{sp}}{m_t} \times 100\% \quad (1)$$

where n_{SPR} is the sand production rate, m_{sp} is the fine sand particle mass of sand production, and m_t is the mass of fine particles flowing into the chip.

In gas-free flow experiments, we conducted multiple control groups with different experiment variables, and due to the stable nature of the results from gas-free flow experiments across multiple tests, we did not set up repetitive trials.

Figure 6 shows the group I test real-time curve, i.e., the relationship between inlet pressure, cumulative suspension mass, and time. The inlet pressure of basic group 1 was maintained at a relatively low level with little fluctuation during the entire test process. The cumulative discharged suspension mass increased linearly, indicating that the seepage flow was stable during the test, and the liquid continued to flow out at the outlet without blockage. The inlet pressure curve and the cumulative discharge suspension mass curve of the 1% and 5% fine particle concentrations are basically the same as those of typical test results with the fine particle concentration of 3%. The seepage flow is stable during the test without blockage. So, the curve will not be given here. In the early and middle stages of the test, the curve is consistent with the typical test result; however, when the test proceeds to about 3250 s, the inlet pressure rises at a higher slope, and there is no liquid flowing out of the solid–liquid collector, and the mass remains unchanged. It is observed through the microscope that the flow in the chip gradually slows down within a few seconds, and finally stops flowing, indicating that there is a blockage, and the liquid cannot through the chip seepage. The blockage continues until the end of the test.

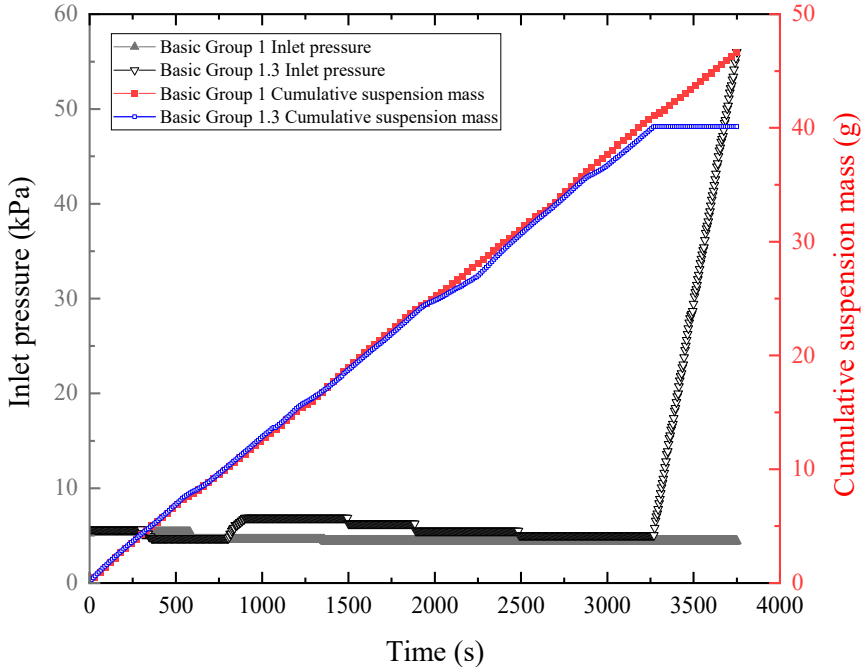

Figure 6. Group I test real-time curve.

No blockage occurred in the four experiments in the second group II in Table 1. The inlet pressure curve and cumulative discharged suspension mass curve of each group are similar to the typical test results in Figure 6, except that the slope of the cumulative discharged suspension mass curve is different. Therefore, no curve is given here.

Fluids move fine particles mainly by applying drag force to them. Stokes drag force can be calculated using Equation (2), given below [37]. In addition, the particle force will be discussed in detail in "Section 4 Discussion".

$$F_{\text{drag}} = \frac{1}{2} C_{\text{D}} A_{\text{fines}} \rho_{\text{fluid}} v_{\text{rel}}^2 \tag{2}$$

where F_{drag} is the drag force of the fluid on the fine particles, C_{D} is the drag coefficient that is related to the fluid viscosity, A_{fines} is the projected area of the contact surface between the fluid and a fine particle in the flow direction, ρ_{fluid} is the fluid density, and v_{rel} is the relative velocity between the fluid and the fine particles.

It can be seen that changing the flow rate will change the drag force of the fluid on the fine particles, which will have a greater impact on the migration of the fine particles. Therefore, some insight into sand control can be obtained. When making a mining strategy, sand production and mining rate should be balanced. Blindly pursuing a higher mining rate may lead to serious sand overproduction, while choosing a moderate mining rate can control sand production and achieve stable gas production. This conclusion is also supported by numerical simulation results [16,17] and indoor experiments [37].

The clogging occurs under the condition of 10% fine particle concentration, while the other concentrations are not clogged. The real-time curve of the test with a fine particle concentration of 10% is shown in Figure 7. Both sets of tests showed blockage at the end of the test, and the blockage continued until the end of the test.

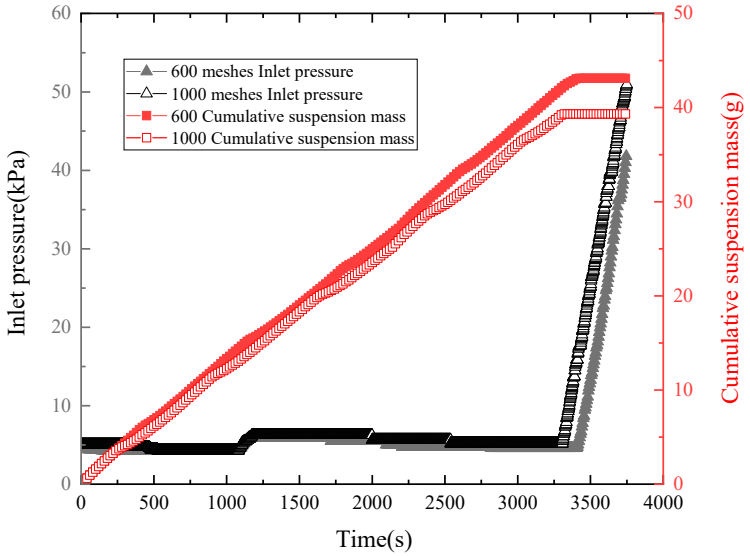

Figure 7. Real-time curve of the 10% fine particle concentration under different particle sizes.

Figure 8 shows the sand production results of fine particles of different particle sizes. The test results of the 600-mesh and 1000-mesh particle sizes differ from the 300-mesh particle size test results. The sand output rate of the 300-mesh particle size continues to decrease as the concentration increases. The sand production rate of 600-mesh and 1000-mesh particles tended to be stable and even increased. It is speculated that the reason is that for the concentration of 10%, due to the small particle size of the 600-mesh and 1000-mesh fine particles, the ratios of the fine particle diameter to the pore channel width *d/o* are 0.07 and 0.04, respectively. The classification cannot cause sand arch clogging, so the impact of fine particle accumulation caused by the increase in concentration is limited. On the other hand, the ratio of *d/o* for the particle size of 300 mesh is 0.14, which can cause sand arch clogging, so the accumulation of fine particles is more serious. This is consistent with previous studies [29,32–34]. It can be observed in the microscope image that the fine particles with a particle size of 600 mesh and 1000 mesh accumulate less in the corner flow area, and there is no high concentration area, while the fine particles with the size of 300 mesh have more serious accumulation, and there appears a darker high-concentration area.

It can be seen that when the concentration of fine particles is higher, the impact of the particle size on sand production is more significant. As the concentration increases, the sand production rate of fine particles with a smaller particle size first decreases and then stabilizes or even increases. The sand production rate of larger fine particles continues to decrease. Therefore, special sand control measures should be taken for small fine particles. Otherwise, severe sand production may be caused when the concentration of fine particles is high.

In the test groups with different concentrations, the final drying collected sand mass and sand production rate are quite different, as shown in Figure 9a. The sand mass varies with the concentration of fine particles. As the sand production mass increases with the increase in fine particle concentration, the increase rate has a gradually decreasing trend. Correspondingly, the sand production rate gradually decreases with the increase in fine particle concentration. Under different fluid flow rate conditions, the final drying collected sand mass and sand production rate are shown in Figure 9b. The sand production mass and sand production rate increase with the increase in the flow velocity, which further proves that as the fluid velocity increases, the motion capacity of fluid carrying fine particles is improved accordingly, which is consistent with the Stokes formula for calculating drag force. The influence of fine particle size on sand production mass and sand production rate is shown in Figure 9c. With the decrease in the fine particle size, the sand production mass and sand production rate have increased.

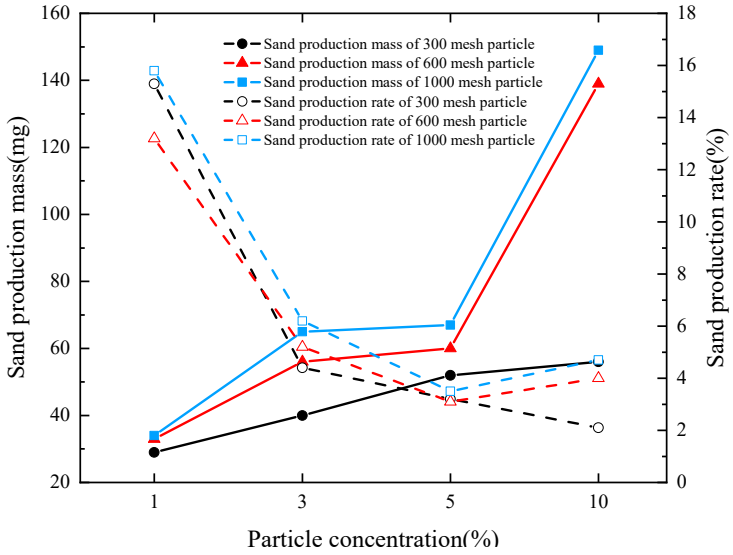

Figure 8. Sand production mass and sand production rate of 600-mesh and 1000-mesh particles under different concentrations.

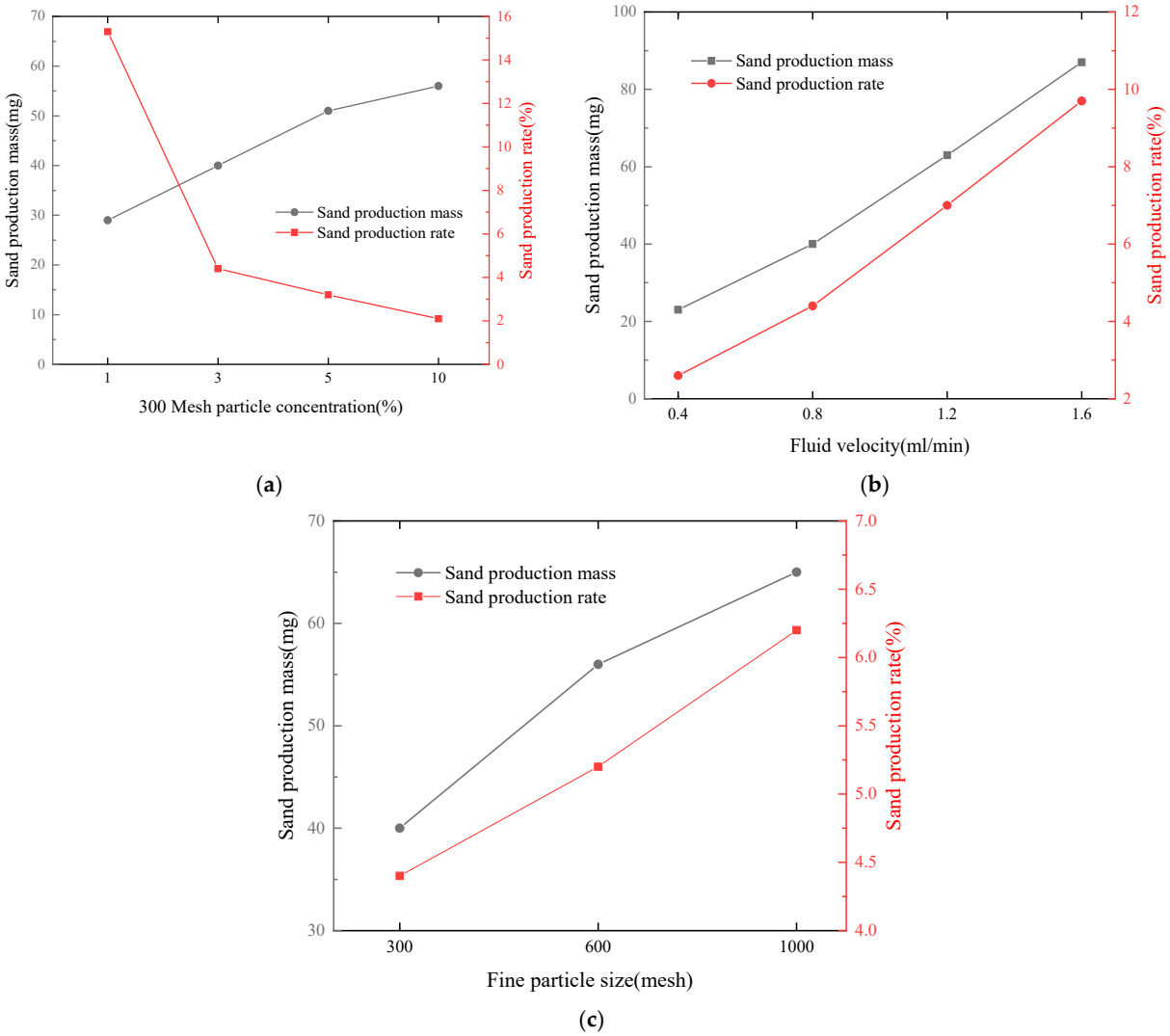

Figure 9. Sand production mass and sand production rate: (**a**) 300-mesh particle concentration; (**b**) fluid velocity; (**c**) fine particle size.

3.1.2. Pore-Scale Migration Patterns

After the solution containing fine particles enters the chip, it first flows diagonally from the main flow area to the outlet to form a liquid-phase percolation channel to separate the gas phase in the chip. The liquid phase flows mainly along the previously formed seepage channel. As more and more liquid enters the chip, the residual gas phase in the chip is gradually dissolved or displaced by the liquid phase, and the liquid seepage channel gradually expands to the corner flow area. After the gas phase inside the chip gradually dissolves to the solubility limit, it can no longer be dissolved in the liquid phase, and finally stays in the chip in the different forms of bubbles, i.e., circles, arcs, crosses, etc., as shown in Figure 10. The bubbles are randomly distributed in every corner of the chip. The bubbles trapped in the chip have a greater impact on the movement of fine particles. The trapped bubbles will affect the flow of the liquid phase and change the seepage path of the liquid phase. Due to the transport of the fine particles mainly relying on the flow of the liquid phase, the trapped air bubbles will significantly affect the migration of fine particles.

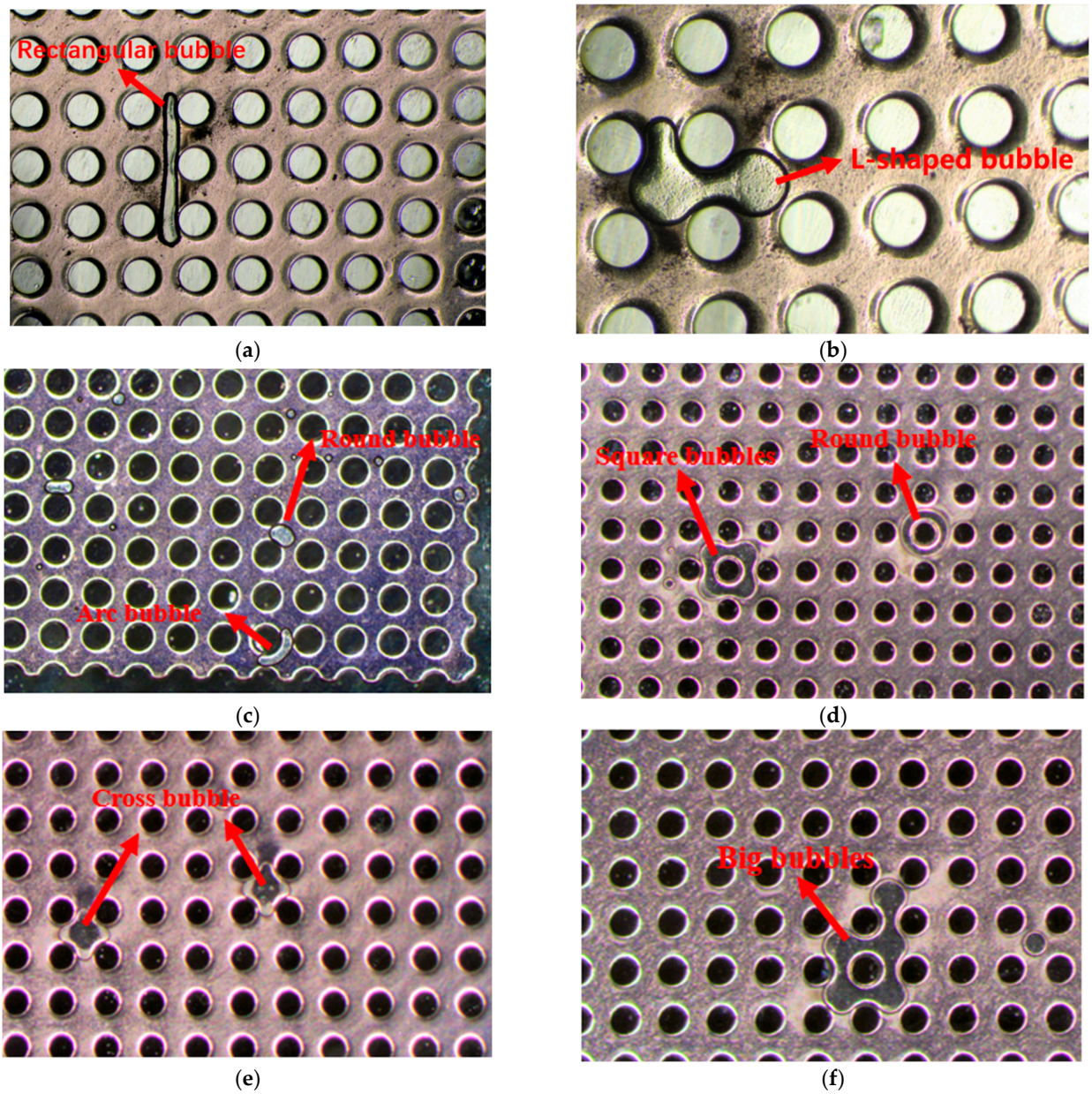

Figure 10. Different shapes of CO_2 bubbles: (**a**) rectangular bubble; (**b**) l-shaped bubble; (**c**) arc and round bubble; (**d**) square and round bubble; (**e**) cross bubble; (**f**) big bubble.

Different shapes of bubbles have different effects on the transport of fine particles, classified by whether the bubbles completely block the pore channel. Some larger bubbles will directly and completely block the pores. The bubbles and pores together form a closed structure similar to a "dead alley". After the fine particles enter such a blind alley with the water flow, the fine particles will gradually be deposited here because of the decrease in the water flow velocity. Because the liquid flows tend to avoid congestion areas, it is difficult for the fine particles deposited here to be taken out by the water flow. As time goes by, the fine particles gradually accumulate to form a high-concentration area, as shown in Figure 11a. The accumulation degree of fine particles is closely related to the length of the dead end composed of bubbles and pores. The longer the length of the dead end, the easier it is for fine particles to accumulate. Although some smaller bubbles cannot completely block the pores and do not form a closed structure similar to a "dead alley", they still impact the migration of fine particles. This is mainly due to the presence of stagnant air bubbles reducing the width of the pore channel, narrowing the seepage channel, and the fine particles being able to form an arch bridge and gradually accumulate in the narrower channel, forming a high concentration area and blocking the pore channel, as shown in Figure 11b.

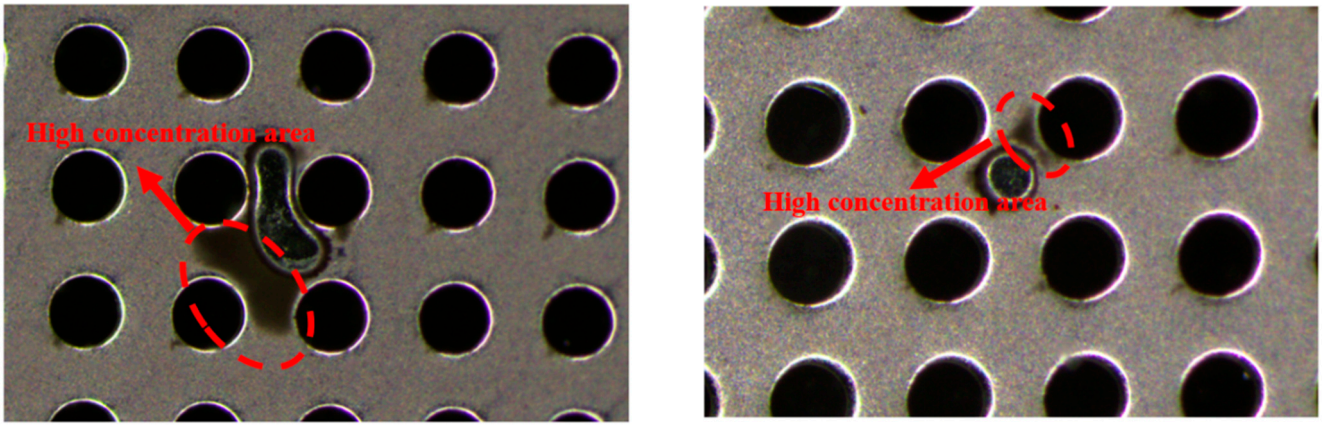

(**a**) (**b**)

Figure 11. Air bubbles cause fine particles to accumulate: (**a**) air bubbles completely block the pores; (**b**) air bubbles do not completely block the pores.

The accumulation of fine particles in different flow areas in the microscopic percolation chip was not the same during the experiment. In the main flow area, due to the large liquid phase flow rate, the faster the flow rate, and the less streamlined bending, the liquid phase has a powerful ability to drive the migration of fine particles. Although there is a small number of fine particles deposited in the main flow area, it is difficult for the fine particles to accumulate to form a high-concentration area. In the corner flow area, due to the flow velocity of the liquid phase being relatively slower, and the streamlines at the corners being more tortuous, the liquid phase has a weak ability to drive fine particles, and fine particles are prone to accumulate to form a high-concentration situation. As shown in Figure 12, in the corner flow area, fine particles first accumulate on the front contact surface between the flow direction and the cylinder in the chip and near the gas–liquid interface, and then gradually accumulate, and the mean gray values of the image decrease gradually. The areas of high concentration where fine particles have accumulated have deepened in color, gradually expanded, and finally formed a significant accumulation, as shown by the red dotted circle in Figure 12. The results provide some suggestions for in situ exploitation, such that it is advisable to introduce some bends in transport pipelines as these bends induce changes in flow direction, leading to the settlement of fine particles. Similarly, in reservoir settings, introducing bends around production wells makes the radial flow bends help to separate fine particles.

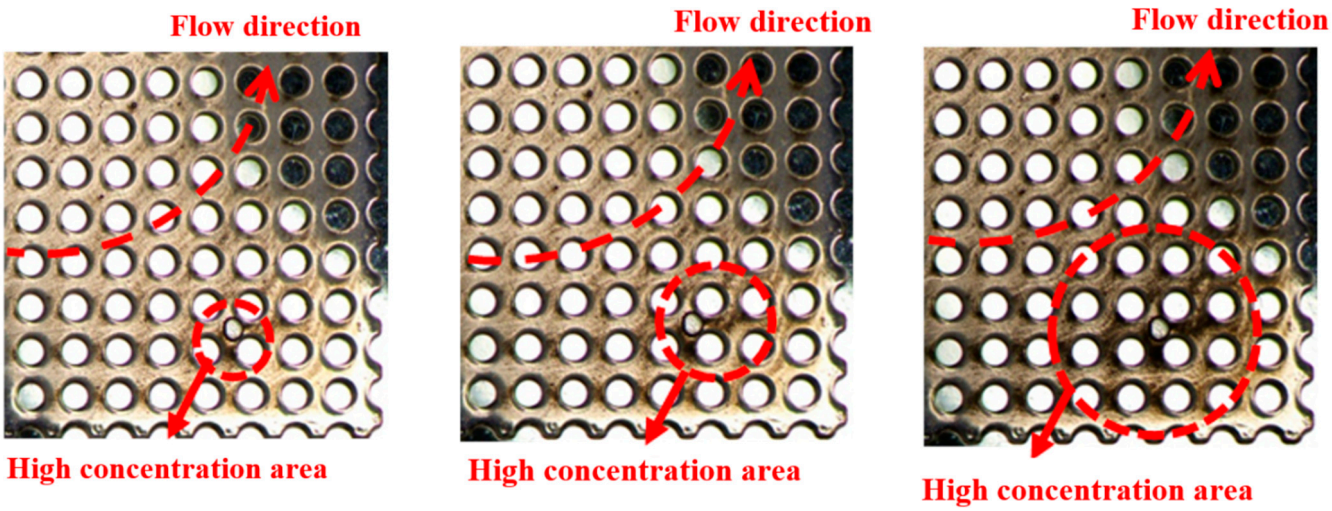

Figure 12. The accumulation of fine particles in the corner flow area at different times: (**a**) t = 10 min, mean gray value = 155; (**b**) t = 15 min, mean gray value = 143; (**c**) t = 20 min, mean gray value = 120.

3.2. Impact of Gas Flow on Particle Migration

3.2.1. Typical Experimental Results

Group 5.1 is selected as a typical test result for detailed analysis in Table 1. It can be seen from Figure 13 that the curve fluctuates greatly throughout the test process. In the initial stage of the test, the inlet pressure remained unchanged, the cumulative discharge suspension mass continued to increase, and the outlet continued to emit gas. When the test was conducted at about 1600 s, the inlet pressure began to rise rapidly, and at the same time, the cumulative discharged suspension mass remained unchanged, and the instantaneous gas flow rate dropped to 0, indicating that no gas–liquid outflow occurred at this time due to blockage. When the test was carried out until about 2200 s, the inlet pressure continued to rise to about 70 kPa, the inlet pressure suddenly began to drop rapidly, while the cumulative discharged suspension mass increased greatly, and the instantaneous gas flow rate was also larger, indicating that the blockage was dredged. High-pressure gas and liquid flow out at a higher rate, resulting in a sudden drop in inlet pressure. After the dredging lasted for a short time, the inlet pressure rose again, resulting in a second blockage occurred. The second blockage lasted until about 2800 s and the inlet pressure increased to 136 kPa, and then the second dredging began, and a large amount of gas and liquid flowed out. Then, there was a third blockage. The inlet pressure continued to rise to 170 kPa and then the third blockage was dredged, followed by a fourth blockage. This blockage continued until the end of the test, and the final inlet pressure reached 460 kPa.

Most of the gas–solid–liquid mixture flows diagonally from the main flow zone toward the outlet, while a small portion flows through the corner flow zone. The two types of flow conditions alternately affect the two-phase fluid flow of the gas–solid–liquid: (1) in the gas–liquid two-phase mixed flow, gas in the form of small bubbles flows together with the liquid into the chip after the flow gradually spreads open. The gas and the liquid are separated, and the small bubbles gradually converge to form a larger volume of bubbles. Large bubbles are separated from the liquid phase. The subsequent gas–liquid phases entering the chip also undergo the process of separation and convergence, and the gas–liquid phases that enter the chip after convergence push their respective phase states to move forward in the chip. As the gas and liquid move forward alternately, the occurrence of the gas–liquid phase in the chip is always changing, and the fine particles are continuously pushed and moved by the gas–liquid two-phase alternately. When the gas–liquid interface passes through the fine particles, due to the existence of the interfacial tension, the fine particles are pushed to move significantly, and it is difficult for them to remain for a long time. (2) The gas–liquid two-phase flow is separated, and there is a single-phase state

occupying the flow channel. After the phase state occupying the flow channel enters the chip, it pushes the other phase state to the flow direction on both sides and then moves forward, establishing a stable flow path between the chip inlet and the outlet, until the other phase enters the chip, breaking the stable flow state. When the liquid phase occupies the flow channel, there is a stable liquid phase percolation path, and the fine particles can move with the flow of the liquid phase. However, when the gas phase occupies the flow channel, the liquid phase stays in the chip and does not flow, and the fine particles do not migrate. In addition, when the gas phase occupies the flow channel and pushes the liquid phase away from both sides of the flow direction, the fine particles migrate obviously due to the existence of interfacial tension, and more fine particles accumulate at the gas–liquid junction, as shown in Figure 14.

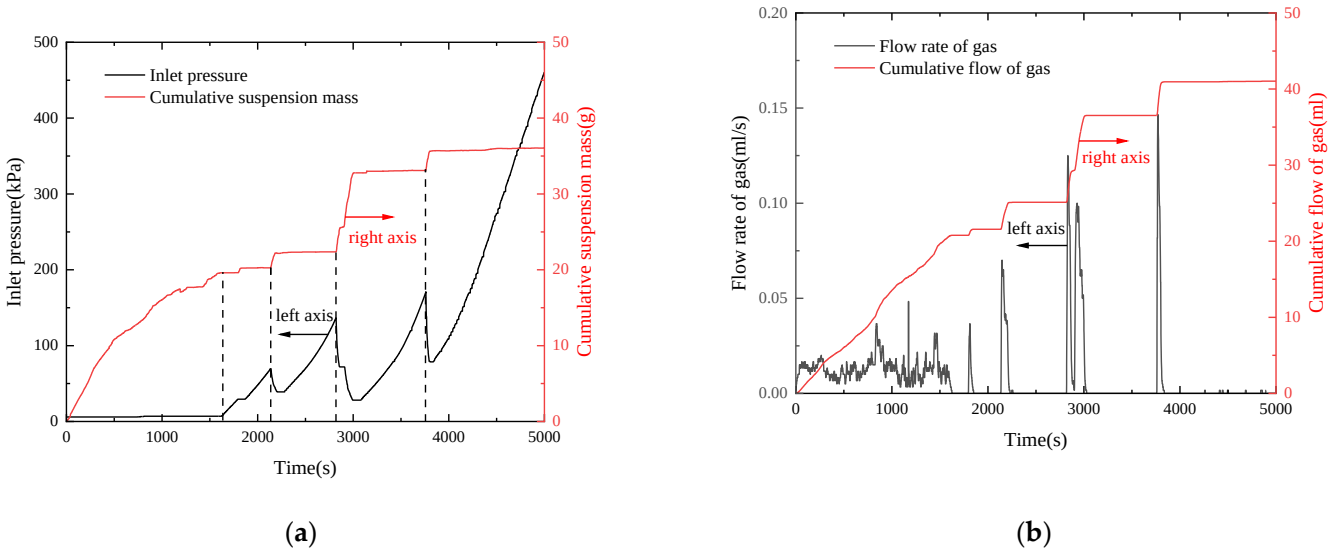

(**a**) (**b**)

Figure 13. The real-time curve of test group 5.1. (**a**) Real-time curve of inlet pressure and cumulative discharged suspension quality; (**b**) real-time curve of gas flow.

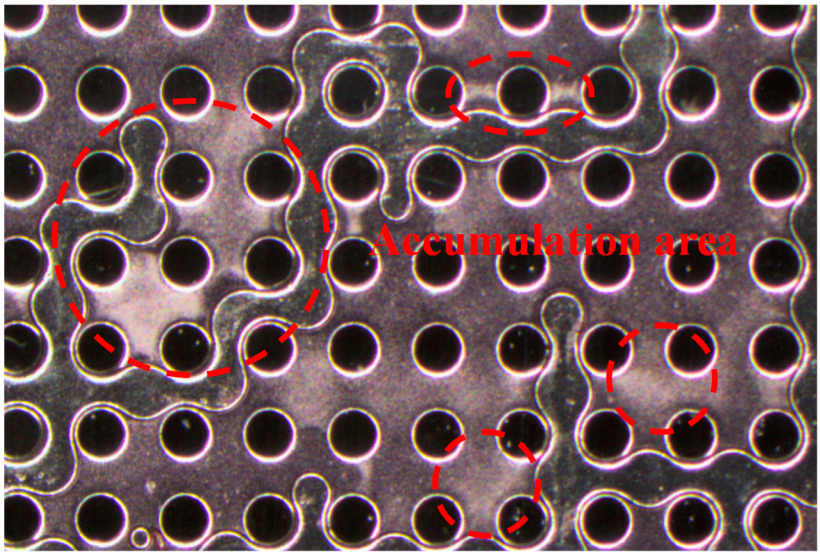

Figure 14. Accumulation area of fine particles at the gas–liquid junction.

3.2.2. The Influence of the Gas–Liquid Ratio

It can be seen from Figure 15 that the test results are different under the same conditions of water and air in comparison with group 5.1 and group 5.2 in Table 1. Test group 5.2 was blocked at about 2200 s. When the inlet pressure rose to 50 kPa to dredge, a large amount of gas and liquid was discharged. After dredging, the inlet pressure remained stable and somewhat higher than in the initial period. It is speculated that although the blockage is dredged, the pores are still partially filled with fine particles, and the inlet pressure increases accordingly as the porosity decreases. During the subsequent test, the blockage no longer appeared, and the gas and liquid flowed out steadily until the end of the test. After the test, after deducting the pre-filled clean water in the outlet pipe, 49.9 g of the solid–liquid mixture was collected. After drying and weighing, the mass of fine particles produced was 84 mg, corresponding to a sand production rate of 9.3%.

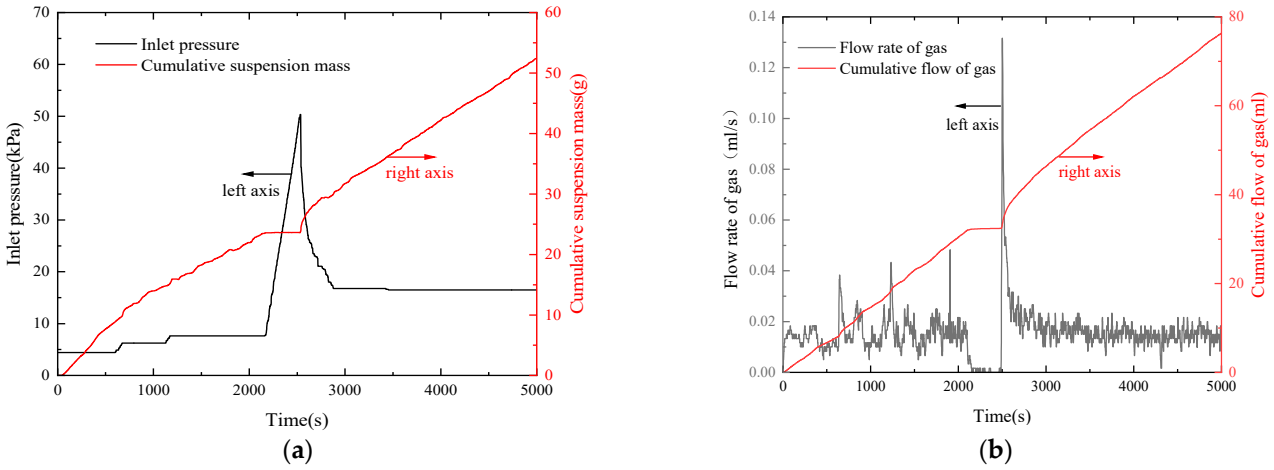

Figure 15. The real-time curve of test group 5.2: (**a**) inlet pressure and cumulative discharge suspension quality curve; (**b**) real-time curve of gas flow.

The real-time curves of test group 5.3 and test group 5.4 are shown in Figure 16. The two groups of experiments with the same gas–liquid ratio also showed different experimental results. Test group 5.3 had a total of three blockages and two dredgings. After the last blockage, the inlet pressure peaked at 603 kPa and then began to decline slowly. During the third blockage process, it was observed through the microscope that a small amount of gas and liquid continued to penetrate the chip through the blockage. The cumulative discharge suspension mass increased by about 2 g in 3700s, and finally, a total of 22.0 g solid–liquid mixture was collected. The mass of fine particles produced was 50 mg, and the sand production rate was 12.6%. Unlike test group 5.3, test group 5.4 did not experience blockage in the early stage of the test. The first blockage did not occur until about 5500 s, and it was blocked directly until the end of the test. The final inlet pressure was 445 kPa and a total of 41.1 g of the solid–liquid mixture was collected. The mass of fine particles produced was 83 mg, and the sand production rate was 11.2%.

The real-time curves of test group 5.5 and test group 5.6 in Table 1 are shown in Figure 17. Both sets of tests were stopped because the inlet pressure reached the device protection pressure of 800 kPa. In test group 5.5, the first blockage occurred at about 2800 s, and the second blockage occurred after dredging. After the second blockage was briefly dredged at about 7000 s, it was blocked again. Then, the inlet pressure continued to rise to the device protection pressure of 800 kPa. The test stopped at about 8700 s, and finally, a total of 12.5 g of the solid–liquid mixture was collected, the mass of fine particles produced was 50 mg, and the sand production rate was 22.2%. The first blockage of test group 6 occurred at about 5800 s. When it was about 7000 s, the inlet pressure appeared to be a flat period, and the cumulative discharged suspension mass increased rapidly, indicating that the flow was smooth at this time, and then the inlet pressure continued

to rise quickly. The dredging occurred again at 11,000 s, and the cumulative discharged suspension mass and gas flow increased. Then, the inlet pressure continued to rise, but gas and liquid continued to flow into the chip through the blockage. The cumulative discharged suspension mass increased by approximately 2.3 g within 2700 s. Therefore, the pressure rises slowly, reaching the device protection pressure of 800 kPa at 14,700 s. The test was stopped, and a total of 25.0 g of the solid–liquid mixture was finally collected. The mass of fine particles was 101 mg, and the sand production rate was 22.4%.

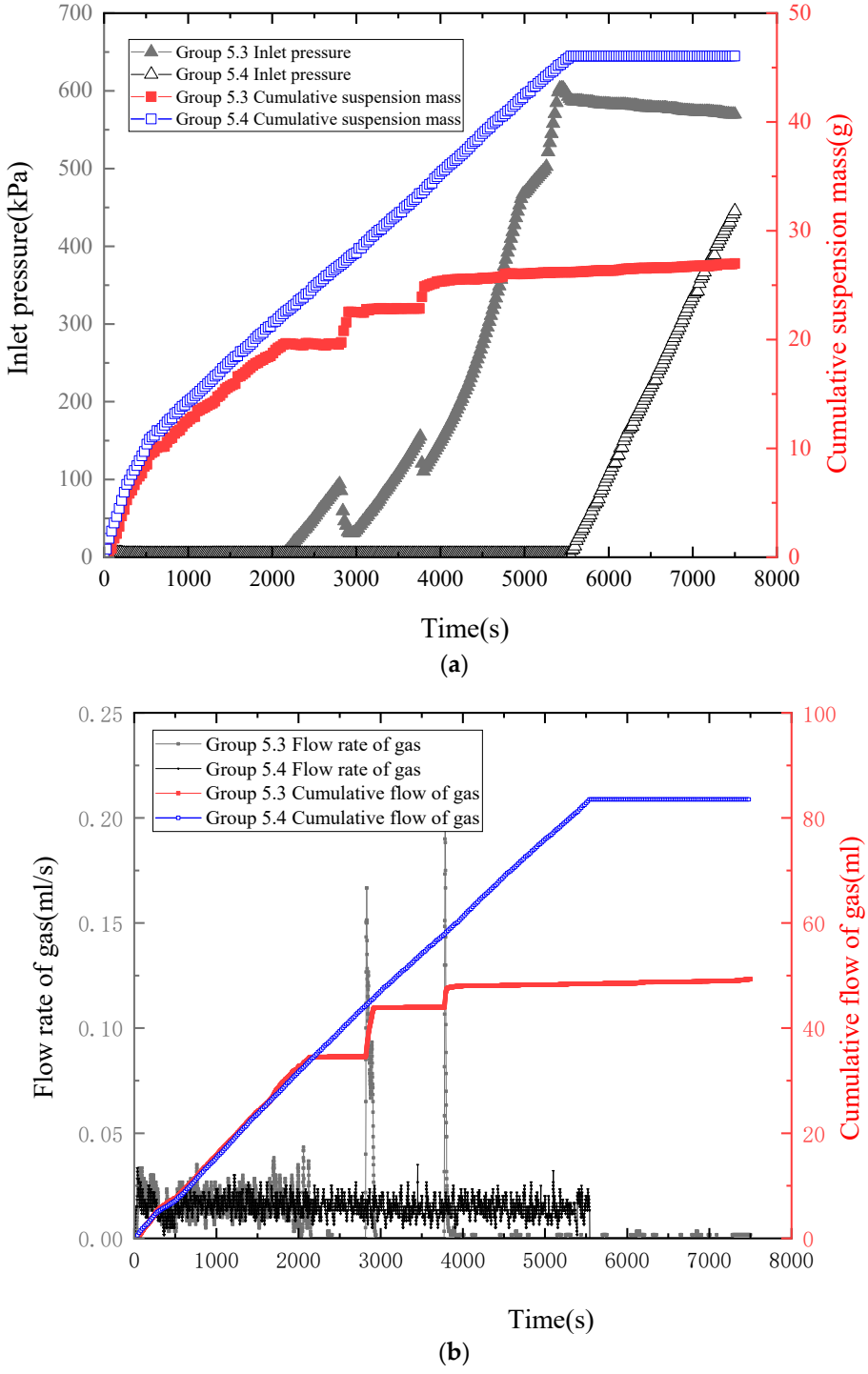

Figure 16. The real-time curves of test groups 5.3 and 5.4: (**a**) inlet pressure and cumulative discharge suspension quality curve; (**b**) real-time curve of gas flow.

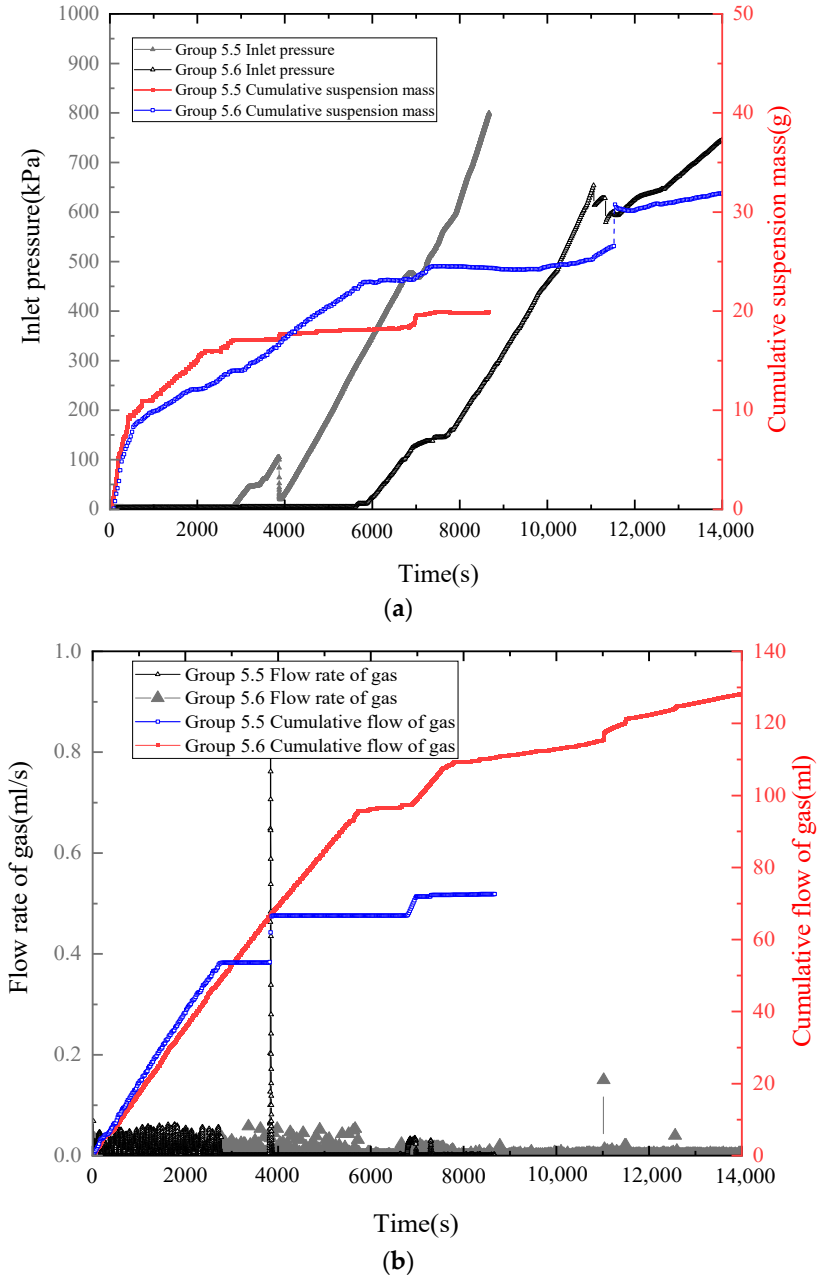

Figure 17. Real-time curves of test group 5.5 and group 5.6: (**a**) inlet pressure and cumulative discharge suspension quality curve; (**b**) real-time curve of gas flow.

It can be seen from the real-time curves of each group that the slope of cumulative suspension mass curves gradually decreases before the blockage, which indicates that as the test progresses, more and more particles remain in the chip, and the overall permeability of the chip is gradually reduced until a blockage occurs. The critical channel for blockage occurs when there is high-concentration aggregation at the gas–liquid interface during alternating gas–liquid flow, leading to clogging when these high-concentration particles reach the pores.

The test results are summarized in Table 2. The results of the six groups of two-phase fluid flow tests show that the blockage of each group is not the same, and the time of the first blockage is relatively random, either early or late. There are also differences in the inlet pressure peak after blockage. On the whole, when the gas–liquid ratio is low, most of the blockages can be dredged, and the peak inlet pressure is relatively low. When the gas–liquid ratio increases, the blockage is not easy to dredge, and the final inlet pressure is

higher. Different clogging conditions lead to great differences in the final sand production mass of the test. Under the same gas–liquid ratio, the final sand production mass of the test group that has clogged earlier is smaller. Therefore, the mass of sand production cannot be directly compared, and the sand production rate can be used to reflect the sand production situation.

As the gas–liquid ratio increases, the sand production rate increases significantly, which is presumed to be due to the following reasons: when the gas–liquid ratio is low, the liquid content is higher and the liquid phase flow is dominant, making the gas–liquid alternate scouring and migration effect of fine particles not obvious; however, with the increase in the gas–liquid ratio, the content of liquid phase decreases, and the alternate scouring effect of gas–liquid is obvious, which drives the migration of a large number of fine particles, so the sand production rate is higher. The microscopic image of the corner flow area is shown in Figure 18. It can also be seen that as the gas–liquid ratio increases, the accumulation of fine particles is gradually reduced, and there is no obvious accumulation of fine particles under the condition of a gas–liquid ratio of 3:1. Therefore, certain insight into sand control can be obtained. When exploiting methane hydrate, it is necessary to control the rate of gas production from hydrate decomposition, select a reasonable rate of gas production, reduce the gas–liquid ratio of the fluid, and reduce sand production.

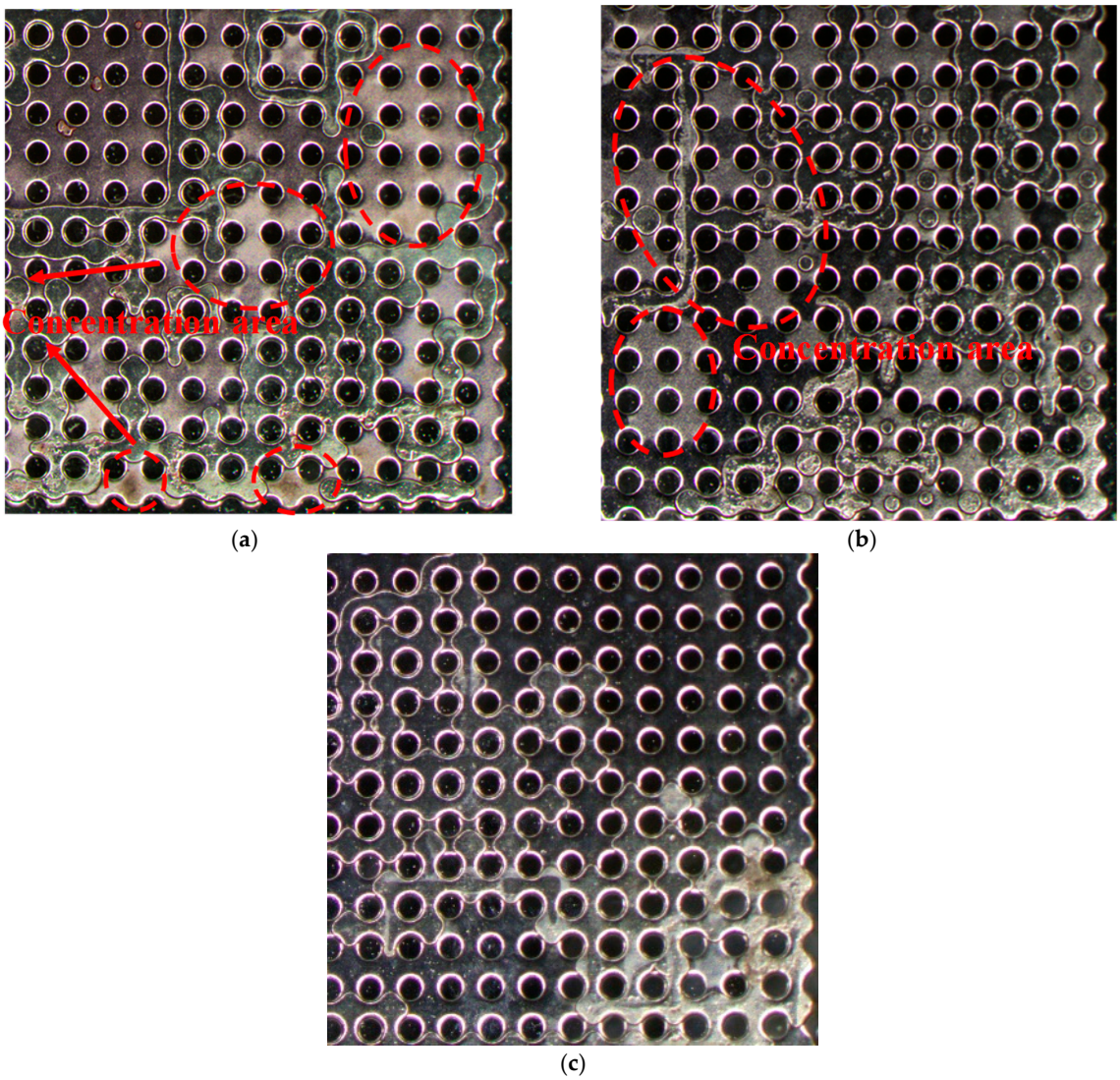

(**a**) (**b**)

(**c**)

Figure 18. The accumulation of fine particles in the corner flow area with different gas–liquid ratios: (**a**) gas–liquid ratio 1:3; (**b**) gas–liquid ratio 1:1; (**c**) gas–liquid ratio 3:1.

Table 2. Summary of test results of two-phase fluid flow.

Group	The Volume of Solution Flowing into the Chip (mL)	Mass of Fine Particles Flowing into the Chip (mg)	Solid Load (mg/min)	Gas Load (ml/min)	Mass of Fine Sand Particles (mg)	Sand Production Rate (%)	Peak Inlet Pressure (kPa)	Time to First Blockage (s)	Blockage
1	33.5	603	24	0.2	58	9.6	460	1632	After multiple blockages, the blockage will be cleared until the end of the test
2	49.9	898	24	0.2	84	9.4	50	2165	Flow steadily after the first blockage and dredging to the end of the test
3	22.0	396	24	0.4	50	12.6	603	2152	After multiple blockages and dredging, the inlet pressure reaches the peak value and then slowly drops
4	41.1	740	24	0.4	83	11.2	445	5549	No dredging after blockage
5	12.5	225	24	0.6	50	22.2	800	2821	After the first blockage, the inlet pressure continues to rise to the protection pressure
6	25.0	450	24	0.6	101	22.4	800	5705	After the blockage, gas, and liquid continue to flow through the blockage, and the inlet pressure slowly rises to the protection pressure

4. Discussion

As shown in Figure 19, different forces acted on a fine particle at the particle level during the experimental tests: (a) a single water-phase flow, (b) a two-phase flow, (c) a particle with the maximum interfacial tension force, and (d) a particle with a planar meniscus parallel to the flow direction. In the state of two-phase flows, with a different angle β from the x-direction to the tangential line of the smooth particle surface at contact with the meniscus, the interfacial tension will obtain the maximum value as the β tends to zero. θ is the dynamic contact angle of the water–gas–solid interface.

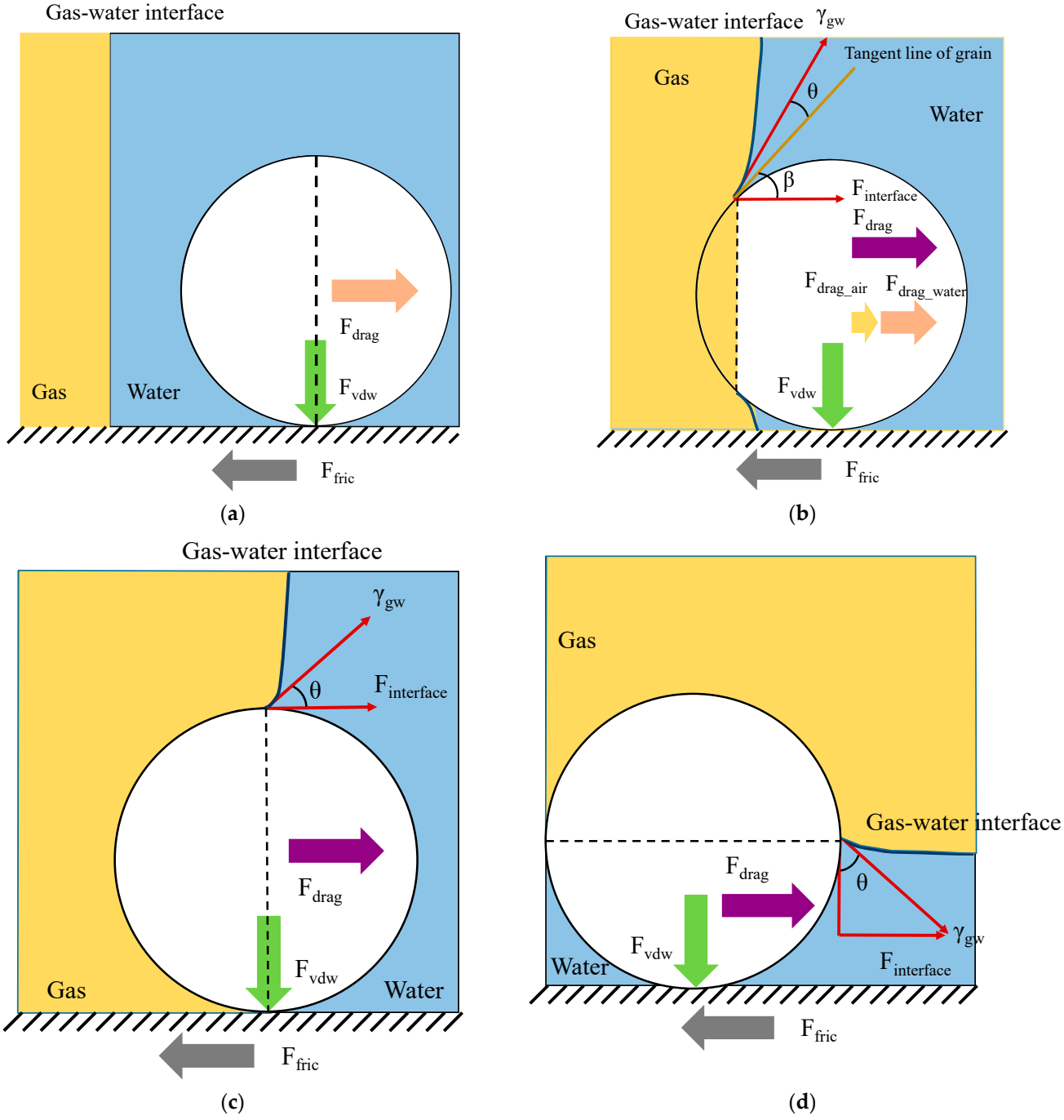

Figure 19. Particle-level forces: (**a**) a single water-phase flow; (**b**) two-phase flows; (**c**) a particle with the maximum interfacial tension force; (**d**) a particle with a planar meniscus parallel to the flow direction.

The Reynolds number can be expressed as [38]:

$$\mathrm{Re} = \frac{\rho_{\mathrm{fluid}} \mathrm{v}_{\mathrm{rel}} d_{\mathrm{fines}}}{\mu_{\mathrm{fluid}}} \tag{3}$$

where ρ_{fluid} is the fluid density, the density of water and air are $\rho_{water} = 1000\ \mathrm{kg/m^3}$ and $\rho_{air} = 1.29\ \mathrm{kg/m^3}$, respectively; μ_{fluid} is dynamic viscosity coefficient, the viscosity coefficients of water and air are $\mu_{\mathrm{water}} = 1 \times 10^{-3}\ \mathrm{p_a \cdot s}$ and $\mu_{air} = 1.8 \times 10^{-5}\ \mathrm{p_a \cdot s}$, respectively, shown in Table 3; v_{rel} is the velocity of the flow field.

Table 3. Variable used in particle-level theoretical analysis.

	Value	Unit
Viscosity of air (μ_{air})	1.8×10^{-5}	$\mathrm{p_a \cdot s}$
Viscosity of water (μ_{water})	1×10^{-3}	$\mathrm{p_a \cdot s}$
Friction coefficient (μ_s)	1	-
Fines density (ρ_{fines})	2.65×10^3	$\mathrm{kg/m^3}$
Sand density (ρ_{sand})	2.65×10^3	$\mathrm{kg/m^3}$
Fluid density (ρ_{fluid})	1000	$\mathrm{kg/m^3}$
Gravitational acceleration (g)	9.81	$\mathrm{m/s^2}$
Gas–water interfacial tension (γ_{gw})	0.072	N/m
Water–gas–solid dynamic contact angle (θ)	30	°

Then the drag coefficient C_D can be expressed by $C_D = \frac{24}{\mathrm{Re}}$ [38], where Re is the Reynolds number. C_D is listed in Table 4.

v_{rel} can be calculated under different values Q_{fluid}, i.e., 0.2 mL/min, 0.4 mL/min, 0.6 mL/min, 0.8 mL/min, 1.2 mL/min, and 1.6 mL/min listed in Table 1. For example, if the fluid flow is $Q_{\mathrm{fluid}} = 0.8\ \mathrm{mL/min} = 0.013\ \mathrm{mL/s} = 1.3 \times 10^{-8}\ \mathrm{m^3/s}$, the cross-section S is 350 μm × 150 μm, then v_{rel} can be calculated:

$$v_{rel} = \frac{Q_{fluid}}{S} = \frac{1.3 \times 10^{-8}}{3.5 \times 10^{-4} \times 1.5 \times 10^{-4}} = 0.254\ \mathrm{m/s} \tag{4}$$

A_{fines} can be calculated:

$$A_{\mathrm{fines}} = \frac{1}{2} S_{\mathrm{fines}} = \frac{1}{2} 4\pi {R_{\mathrm{fines}}}^2 \tag{5}$$

Therefore, $F_{\mathrm{drag\_water}}$ and $F_{\mathrm{drag\_air}}$ can be calculated based on Equation (2) by using the parameters C_D, A_{fines}, ρ_{fluid}, and v_{rel}, listed in Table 4.

In the experimental tests, the gas–liquid interface is mainly vertical, the interfacial force can be calculated [38]:

$$F_{\mathrm{interface1}} = C_{\mathrm{interfact}} \gamma_{\mathrm{gw}} \cos\theta \tag{6}$$

where $C_{\mathrm{interfact}}$ is the circumferential length based on the gas and water interface.

When the gas–liquid interface is horizontal, the interfacial force can be calculated:

$$F_{\mathrm{interface2}} = C_{\mathrm{interface}} \gamma_{\mathrm{gw}} \sin\theta \tag{7}$$

When γ_{gw} is equal to be 0.072 N/m in Reference [37], the contact angle is $\theta = 30°$, the maximum of the interfacial tension can be calculated using Equation (6), as shown in Table 4.

Table 4. Force analysis of particle level.

Group	Q_{water}	Q_{air}	v_{rel_water}	v_{rel_air}	Re_{water}	Re_{air}	C_{Dwater}	C_{Dair}	A_{fines}	$F_{dragwater}$	$F_{dragair}$	F_{vdw_water}	F_{vdw_air}	$F_{interface1}$	F_{fric_max}	m_{sp}/n_{SPR}
1	0.8	/	0.254	/	12.190	/	1.969	/	3.619×10^{-9}	2.298×10^{-7}	/	6.300×10^{-7}	/	/	6.309×10^{-7}	40 (4.4%)
1.1	0.8	/	0.254	/	12.190	/	1.969	/	3.619×10^{-9}	2.298×10^{-7}	/	6.300×10^{-7}	/	/	6.309×10^{-7}	29 (15.3%)
1.2	0.8	/	0.254	/	12.190	/	1.969	/	3.619×10^{-9}	2.298×10^{-7}	/	6.300×10^{-7}	/	/	6.309×10^{-7}	52 (3.2%)
1.3	0.8	/	0.254	/	12.190	/	1.969	/	3.619×10^{-9}	2.298×10^{-7}	/	6.300×10^{-7}	/	/	6.309×10^{-7}	56 (2.1%)
2	0.8	/	0.254	/	12.190	/	1.969	/	3.619×10^{-9}	2.298×10^{-7}	/	6.300×10^{-7}	/	/	6.309×10^{-7}	40 (4.4%)
2.1	0.4	/	0.127	/	6.095	/	3.978	/	3.619×10^{-9}	1.149×10^{-7}	/	6.300×10^{-7}	/	/	6.309×10^{-7}	23 (2.6%)
2.2	1.2	/	0.381	/	18.286	/	1.313	/	3.619×10^{-9}	3.447×10^{-7}	/	6.300×10^{-7}	/	/	6.309×10^{-7}	63 (7.0%)
2.3	1.6	/	0.508	/	24.381	/	0.984	/	3.619×10^{-9}	4.596×10^{-7}	/	6.300×10^{-7}	/	/	6.309×10^{-7}	87 (9.7%)
3	0.8	/	0.254	/	5.841	/	4.109	/	8.310×10^{-10}	1.101×10^{-7}	/	3.019×10^{-7}	/	/	3.020×10^{-7}	56 (5.2%)
3.1	0.8	/	0.254	/	5.841	/	4.109	/	8.310×10^{-10}	1.101×10^{-7}	/	3.019×10^{-7}	/	/	3.020×10^{-7}	33 (13.2%)
3.2	0.8	/	0.254	/	5.841	/	4.109	/	8.310×10^{-10}	1.101×10^{-7}	/	3.019×10^{-7}	/	/	3.020×10^{-7}	60 (3.1%)
3.3	0.8	/	0.254	/	5.841	/	4.109	/	8.310×10^{-10}	1.101×10^{-7}	/	3.019×10^{-7}	/	/	3.020×10^{-7}	139 (4.0%)
4	0.8	/	0.254	/	3.302	/	7.269	/	2.655×10^{-10}	6.223×10^{-8}	/	1.706×10^{-7}	/	/	1.706×10^{-7}	65 (6.2%)
4.1	0.8	/	0.254	/	3.302	/	7.269	/	2.655×10^{-10}	6.223×10^{-8}	/	1.706×10^{-7}	/	/	1.706×10^{-7}	34 (15.8%)
4.2	0.8	/	0.254	/	3.302	/	7.269	/	2.655×10^{-10}	6.223×10^{-8}	/	1.706×10^{-7}	/	/	1.706×10^{-7}	67 (3.5%)
4.3	0.8	/	0.254	/	3.302	/	7.269	/	2.655×10^{-10}	6.223×10^{-8}	/	1.706×10^{-7}	/	/	1.706×10^{-7}	149 (4.7%)
5.1	0.6	0.2	0.190	0.063	9.143	0.218	2.625	109.884	3.619×10^{-9}	1.723×10^{-7}	1.034×10^{-9}	6.300×10^{-7}	6.500×10^{-6}	9.403×10^{-6}	6.501×10^{-6}	58 (9.6%)
5.2	0.6	0.2	0.190	0.063	9.143	0.218	2.625	109.884	3.619×10^{-9}	1.723×10^{-7}	1.034×10^{-9}	6.300×10^{-7}	6.500×10^{-6}	9.403×10^{-6}	6.501×10^{-6}	84 (9.4%)
5.3	0.4	0.4	0.127	0.127	6.095	0.437	3.938	54.942	3.619×10^{-9}	1.149×10^{-7}	2.068×10^{-9}	6.300×10^{-7}	6.500×10^{-6}	9.403×10^{-6}	6.501×10^{-6}	50 (12.6%)
5.4	0.4	0.4	0.127	0.127	6.095	0.437	3.938	54.942	3.619×10^{-9}	1.149×10^{-7}	2.068×10^{-9}	6.300×10^{-7}	6.500×10^{-6}	9.403×10^{-6}	6.501×10^{-6}	83 (11.2%)
5.5	0.2	0.6	0.063	0.190	3.048	0.655	7.875	36.628	3.619×10^{-9}	5.745×10^{-8}	3.102×10^{-9}	6.300×10^{-7}	6.500×10^{-6}	9.403×10^{-6}	6.501×10^{-6}	50 (22.2%)
5.6	0.2	0.6	0.063	0.190	3.048	0.655	7.875	36.628	3.619×10^{-9}	5.745×10^{-8}	3.102×10^{-9}	6.300×10^{-7}	6.500×10^{-6}	9.403×10^{-6}	6.501×10^{-6}	101 (22.4%)

Note: As groups 1–4.3 did not contain air, the related indices are not present.

The van der Waals force F_{vdw} is a distance-dependent interaction between atoms or molecules [39]:

$$F_{vdw} = \frac{HR_{\text{fines}}}{6a^2} \tag{8}$$

where the parameter a indicates the distance between two surfaces. For two solid surfaces in contact, the value of a is equal to be $a = 0.2$nm. R_{fines} is the particle radius, on the basis of mesh in Table 1. H is the Hamaker constant, related to the medium in which the two objects are in contact. The values of H are $H = 0.63 \times 10^{-20}$ J in water and $H = 6.5 \times 10^{-20}$ J in air [39], respectively. The $F_{\text{vdw\_water}}$ and $F_{\text{vdw\_air}}$ can be calculated based on Equation (8) and are listed in Table 4.

The friction can be calculated using the following equation:

$$F_{fric} = \mu_s(F_{vdw} + g(\rho_{fines}V_{fines} - \rho_{fluid}V_{water-wet})) \tag{9}$$

where μ_s is the friction coefficient, and $\mu_s = 1$; $V_{\text{water-wet}}$ is equal to V_{fines} in a single-phase condition, illustrated in Figure 18a. $V_{\text{water-wet}}$ is reducing with the gas–water interface sweeping the fine particles, as shown in Figure 18b–d. As the gas–liquid ratios of groups 5.1–5.6 keep changing, F_{vdw} varies between $F_{\text{vdw\_water}}$ and $F_{\text{vdw\_air}}$. $F_{fric\_\max}$ can be calculated by $F_{\text{vdw\_air}}$ and Equation (9), which are listed in Table 4.

Based on the magnitude analysis of different forces at the particle level, the interfacial force plays a leading role. In the gas-free flow experimental groups, as the particle size decreases, the drag force, interfacial tension, and friction force all decrease, while the parameter of the fine sand particle mass of sand production varies without an apparent pattern. From the perspective of force analysis, the amount of sand production rate is not well connected with the force. The sand production rate is more affected by the blockage of fine particles in the pores. In the gas flow experimental groups, i.e., groups 5.1–5.6, $F_{\text{interface1}}$ is always greater than F_{vdw}, leading to the sand phenomenon. With the increases in the gas–liquid ratio, the sand production rate correspondingly increased due to the gas–liquid ratio. The reason is that fine particles mainly move in the liquid flow, and with the increase in the gas–liquid ratio, the frequency of gas–liquid alternating flow increases, which improves the efficiency of the interfacial force and leads to sand production.

In this study, based on the geological information of hydrate reservoirs in the South China Sea, three kinds of silica sand with different particle sizes were selected for the experiment. Nevertheless, the geological information of hydrate reservoirs in the South China Sea is not the same as that in other regions of the world. First, the average particle size is smaller than other regions; for example, the average particle size of the sea area of Japan is 120 μm [40], which is much larger than that of China. Second, although the mineral composition of each region is roughly the same, including quartz, orthoclase, plagioclase, mica, hornblende, montmorillonite, and so on [41–43], the specific content varies. And different mineral components have an effect on the aggregation of fine particles, and ultimately affect the migration of fine particles [31]. Therefore, it is necessary to carry out experiments according to the geological characteristics of hydrate reservoirs in different regions.

Still, some findings in this study are universally applicable and are independent of geological conditions, i.e., the influence of gas and interfacial tension, the influence of fine particle concentration and fluid flow rate, etc., as similar discoveries can also be found in previous studies with different experimental conditions [21,23,24,37].

5. Conclusions

The main research conclusions are as follows:

(1) The concentration of fine particles has an impact on the migration of fine particles. As the concentration of fine particles increases, the accumulation of fine particles gradually increases, more high-concentration areas appear, and the sand production rate continues to decrease. In the case of occurring accumulation, the fine particles first

accumulate in the front contact surface between the flow direction and the cylinder in the chip and near the gas–liquid interface, and the high-concentration area gradually expanded after the post-accumulation intensified.

(2) Flow velocity influences the migration of fine particles. As the flow rate increases, the movement ability of fluid carrying fine particles is improved accordingly. Fine particles are difficult to accumulate, and the mass and rate of sand production are increased. In the microchip, the area with slow flow velocity and tortuous flow line easily appears as the area with a high concentration of fine particles. Therefore, in actual mining, a high mining rate may lead to significant sand production.

(3) Different fine particle sizes present different sand production patterns. With the decrease in fine particle size, the mass and rate of sand production increase under the same concentration, but the change in the sand production rate of fine particles of different particle sizes is not the same with the increase in the concentration. The sand production rate of 300 mesh (48 μm) fine particles continued to decrease with the increase in concentration. However, when the concentration of 600-mesh (23 μm) and 1000-mesh (13 μm) particles reaches 5%, the sand production rate tends to be stable or even increases.

(4) The presence of the gas phase has a significant influence on the migration of fine particles. In the single-phase fluid flow, the gas in the microchip will gradually dissolve in the liquid phase and eventually remain in the microchip in the form of bubbles. The bubbles affect the migration of fine particles by occupying the pore path, leading to the accumulation of fine particles at the gas–liquid interface, forming a high concentration area. In the two-phase fluid flow, the gas phase has different flow modes. The interfacial tension at the gas–liquid interface during gas–liquid flow can effectively drive the movement of fine particles.

(5) The presence of gas is more likely to lead to clogging and dredging. Under the same test conditions, the single-phase fluid flow will not be clogged, but the two-phase fluid flow will be. After the clogging continues for a period, it will be dredged due to pressure accumulation. During the dredging, the fluid flows rapidly and effectively drives the migration of fine particles. The occurrence of blockage and dredging are relatively random. When the gas–liquid ratio is low, blockages and dredging will occur multiple times, and it will be more difficult to dredge after the gas–liquid ratio increases.

(6) A moderate mining rate is recommended during extraction. A moderate mining rate, on the one hand, can control the speed of gas generation, when the gas content is high, the interfacial tension effectively drives the fine particles, finally resulting in sand production. On the other hand, a moderate mining rate can also control the fluid flow velocity, which significantly impacts the movement of fine particles, and high-speed fluid may cause significant sand production.

The experimental setup still has some limitations for improvement, and future enhancements can be made in the following aspects: (1) The temperature and pressure apparatus can be improved to replicate actual reservoir conditions and methane gas utilized for experiments to simulate the decomposition and reformation of hydrates during the migration process. (2) Fine particles of different mineral compositions and varying particle size distributions should be tested to analyze and summarize the migration law of different fine particles. (3) The actual reservoir pore structure should be scanned and imaged to produce microchip models for experiments so that we can simulate a closer representation of real pore structures, and enable a more realistic simulation of the migration of fine particles within the reservoir.

Author Contributions: Conceptualization, X.H.; methodology, X.H. and P.C.; software, J.H.; validation, J.H. and X.H.; formal analysis, J.H. and X.H.; investigation, X.H. and P.C.; resources, P.C.; data curation, X.H.; writing—original draft preparation, J.H.; writing—review and editing, X.H.; visualization, J.H.; supervision, P.C.; project administration, P.C.; funding acquisition, P.C. All authors have read and agreed to the published version of the manuscript.

Funding: This work was funded by the China Postdoctoral fund (No. 2019M651580) and 2022 Guangxi Polytechnic of Construction Teaching Innovation Team Project "Prefabricated and Intelligent Teaching Innovation Team" (No. GJYR202215).

Institutional Review Board Statement: Not applicable.

Informed Consent Statement: Informed consent was obtained from all subjects involved in the study.

Data Availability Statement: The data presented in this study are available on request from the corresponding author.

Acknowledgments: We would like to thank Professor Fang Liu for her guidance and help in this study.

Conflicts of Interest: The authors declare no conflicts of interest.

Abbreviations

The following symbols are used in this paper:
n_{SPR} = sand production rate;
m_{sp} = fine sand particles mass of sand production;
m_t = mass of fine particles flowing into the chip;
F_{drag} = drag force of the fluid on the fine particles;
C_D = drag coefficient that is related to the fluid viscosity;
A_{fines} = projected area of the contact surface between the fluid and a fine particle in the flow direction;
ρ_{fluid} = fluid density;
v_{rel} = relative velocity between the fluid and the fine particles;
d = fine particles diameter;
o = pore channel width;
β = angle from the x-direction to the tangential line of the smooth particle surface at contact with the meniscus;
θ = dynamic contact angle of the water–gas–solid interface;
Re = Reynolds number;
μ_{fluid} = dynamic viscosity coefficient;
Q_{fluid} = fluid flow;
S = cross-section;
S_{fines} = surface area of fine particles;
R_{fines} = fine particles radius;
F_{drag_water} = drag force of water on the fine particles;
F_{drag_air} = drag force of air on the fine particles;
$F_{interface1}$ = interfacial force when the gas–liquid interface is vertical;
$C_{interfact}$ = circumferential length based on the gas and water interface;
γ_{gw} = gas–water interfacial tension;
$F_{interface2}$ = interfacial force when the gas–liquid interface is horizontal;
F_{vdw} = van der Waals force;
H = Hamaker constant;
a = distance between two surfaces;
F_{vdw_water} = van der Waals force in water;
F_{vdw_air} = van der Waals force in air;
F_{fric} = friction;
μ_s = friction coefficient;
V_{fines} = particles volume;
$V_{water-wet}$ = particles volume when wetted by water;
F_{fric_max} = maximum friction.

References

1. Nisbet, E.G.; Piper, D.J.W. Giant Submarine Landslides. *Nature* **1998**, *392*, 329–333. [CrossRef]
2. Zhang, H.; Lu, H.; Liang, J.; Wu, N. The Methane Hydrate Accumulation Controlled Compellingly by Sediment Grain at Shenhu, Northern South China Sea. *Chin. Sci. Bull. (Chin. Version)* **2016**, *61*, 388. [CrossRef]
3. Xu, C.-G.; Li, X.-S. Research Progress on Methane Production from Natural Gas Hydrates. *RSC Adv.* **2015**, *5*, 54672–54699. [CrossRef]
4. Chibura, P.E.; Zhang, W.; Luo, A.; Wang, J. A Review on Gas Hydrate Production Feasibility for Permafrost and Marine Hydrates. *J. Nat. Gas Sci. Eng.* **2022**, *100*, 104441. [CrossRef]
5. Hassanpouryouzband, A.; Joonaki, E.; Farahani, M.V.; Takeya, S.; Ruppel, C.; Yang, J.; English, N.J.; Schicks, J.M.; Edlmann, K.; Mehrabian, H. Gas Hydrates in Sustainable Chemistry. *Chem. Soc. Rev.* **2020**, *49*, 5225–5309. [CrossRef] [PubMed]
6. Qiu, K.; Yamamoto, K.; Birchwood, A.; Chen, Y. Well-Integrity Evaluation for Methane-Hydrate Production in the Deepwater Nankai Trough. *SPE Drill. Complet.* **2015**, *30*, 52–67. [CrossRef]
7. Terao, Y.; Duncan, M.; Hay, B.; Dang, L. Deepwater Methane Hydrate Gravel Packing Completion Results and Challenges. In Proceedings of the Offshore Technology Conference, Houston, TX, USA, 5–8 May 2014; p. D031S034R007.
8. Chee, S.; Leokprasirtkul, T.; Kanno, T.; Osawa, O.; Sudo, Y.; Takekoshi, M.; Yu, H.; Yamamoto, K. A Deepwater Sandface Monitoring System for Offshore Gas Hydrate Production. In Proceedings of the Offshore Technology Conference, Houston, Houston, TX, USA, 5–8 May 2014. [CrossRef]
9. Yamamoto, K.; Terao, Y.; Fujii, T.; Ikawa, T.; Seki, M.; Matsuzawa, M.; Kanno, T. Operational Overview of the First Offshore Production Test of Methane Hydrates in the Eastern Nankai Trough. In Proceedings of the Offshore Technology Conference, Houston, Houston, TX, USA, 5–8 May 2014; p. D031S034R004.
10. Zhang, W.; Shao, M.; Tian, Q. Technical Progress of a Pilot Project to Produce Natural Gas Hydrate in Japanese Waters. *Pet. Drill. Tech.* **2017**, *45*, 98–102.
11. Fujii, T.; Suzuki, K.; Tamaki, M.; Takayama, T.; Suzuki, S. The Selection of the Candidate Location for the Second Offshore Methane Hydrate Production Test and Geological Findings from the Pre-Drilling Operation, in the Eastern Nankai Trough, Japan. In Proceedings of the 9th International Conference on Gas Hydrates, Denver, CO, USA, 25–30 June 2017; pp. 25–30.
12. Grover, T.; Moridis, G.J.; Holditch, S.A. Analysis of Reservoir Performance of the Messoyakha Gas Hydrate Reservoir. In Proceedings of the SPE Annual Technical Conference and Exhibition, Denver, CO, USA, 21–24 September 2008; p. SPE-114375-MS.
13. Haberer, R.M.; Mangelsdorf, K.; Wilkes, H.; Horsfield, B. Occurrence and Palaeoenvironmental Significance of Aromatic Hydrocarbon Biomarkers in Oligocene Sediments from the Mallik 5L-38 Gas Hydrate Production Research Well (Canada). *Org. Geochem.* **2006**, *37*, 519–538. [CrossRef]
14. Yamamoto, K.; Dallimore, S. Aurora-JOGMEC-NRCan Mallik 2006–2008 Gas Hydrate Research Project Progress. *Nat. Gas Oil* **2008**, *304*, 285–4541.
15. Boswell, R.; Schoderbek, D.; Collett, T.S.; Ohtsuki, S.; White, M.; Anderson, B.J. The Iġnik Sikumi Field Experiment, Alaska North Slope: Design, Operations, and Implications for CO_2–CH_4 Exchange in Gas Hydrate Reservoirs. *Energy Fuels* **2017**, *31*, 140–153. [CrossRef]
16. Zhu, H.; Xu, T.; Yuan, Y.; Feng, G.; Xin, X. Numerical Analysis of Sand Production during Natural Gas Extraction from Unconsolidated Hydrate-Bearing Sediments. *J. Nat. Gas Sci. Eng.* **2020**, *76*, 103229. [CrossRef]
17. Uchida, S.; Klar, A.; Yamamoto, K. Sand Production Model in Gas Hydrate-Bearing Sediments. *Int. J. Rock Mech. Min. Sci.* **2016**, *86*, 303–316. [CrossRef]
18. Ning, F.; Sun, J.; Liu, Z.; Liang, J. Prediction of Sand Production in Gas Recovery from the Shenhu Hydrate Reservoir by Depressurization. In Proceedings of the 9th International Conference on Gas Hydrate, Denver, CO, USA, 25–30 June 2017.
19. Yan, C.; Li, Y.; Cheng, Y.; Wang, W.; Song, B.; Deng, F.; Feng, Y. Sand Production Evaluation during Gas Production from Natural Gas Hydrates. *J. Nat. Gas Sci. Eng.* **2018**, *57*, 77–88. [CrossRef]
20. Yu, L.; Zhang, L.; Zhang, R.; Ren, S. Assessment of Natural Gas Production from Hydrate-Bearing Sediments with Unconsolidated Argillaceous Siltstones via a Controlled Sandout Method. *Energy* **2018**, *160*, 654–667. [CrossRef]
21. Oyama, H.; Nagao, J.; Suzuki, K.; Narita, H. Experimental Analysis of Sand Production from Methane Hydrate Bearing Sediments Applying Depressurization Method. *J. MMIJ* **2010**, *126*, 497–502. [CrossRef]
22. Jung, J.W.; Jang, J.; Santamarina, J.C.; Tsouris, C.; Phelps, T.J.; Rawn, C.J. Gas Production from Hydrate-Bearing Sediments: The Role of Fine Particles. *Energy Fuels* **2012**, *26*, 480–487. [CrossRef]
23. Murphy, A.; Soga, K.; Yamamoto, K. Experimental Investigation into Sand Production from Turbidite Strata. *J. Pet. Sci. Eng.* **2020**, *190*, 107056. [CrossRef]
24. Lu, J.; Xiong, Y.; Li, D.; Shen, X.; Wu, Q.; Liang, D. Experimental Investigation of Characteristics of Sand Production in Wellbore during Hydrate Exploitation by the Depressurization Method. *Energies* **2018**, *11*, 1673. [CrossRef]
25. Okwananke, A.; Hassanpouryouzband, A.; Vasheghani Farahani, M.; Yang, J.; Tohidi, B.; Chuvilin, E.; Istomin, V.; Bukhanov, B. Methane Recovery from Gas Hydrate-Bearing Sediments: An Experimental Study on the Gas Permeation Characteristics under Varying Pressure. *J. Pet. Sci. Eng.* **2019**, *180*, 435–444. [CrossRef]
26. Li, C.; Liu, C.; Hu, G.; Sun, J.; Hao, X.; Liu, L.; Meng, Q.-G. Investigation on the Multiparameter of Hydrate-Bearing Sands Using Nano-Focus X-Ray Computed Tomography. *J. Geophys. Res. Solid Earth* **2019**, *124*, 2286–2296. [CrossRef]

27. Hu, C.; Liu, X.; Jia, Y.; Duan, Z. Permeability Anisotropy of Methane Hydrate-Bearing Sands: Insights from CT Scanning and Pore Network Modelling. *Comput. Geotech.* **2020**, *123*, 103568. [CrossRef]
28. Zhang, C.; Dehoff, K.; Hess, N.; Oostrom, M.; Wietsma, T.W.; Valocchi, A.J.; Fouke, B.W.; Werth, C.J. Pore-Scale Study of Transverse Mixing Induced $CaCO_3$ Precipitation and Permeability Reduction in a Model Subsurface Sedimentary System. *Environ. Sci. Technol.* **2010**, *44*, 7833–7838. [CrossRef] [PubMed]
29. Jung, J.; Cao, S.C.; Shin, Y.-H.; Al-Raoush, R.I.; Alshibli, K.; Choi, J.-W. A Microfluidic Pore Model to Study the Migration of Fine Particles in Single-Phase and Multi-Phase Flows in Porous Media. *Microsyst. Technol.* **2018**, *24*, 1071–1080. [CrossRef]
30. Song, Z.; Zhu, W.; Wang, X.; Guo, S. 2-D Pore-Scale Experimental Investigations of Asphaltene Deposition and Heavy Oil Recovery by CO_2 Flooding. *Energy Fuels* **2018**, *32*, 3194–3201. [CrossRef]
31. Cao, S.C.; Jang, J.; Jung, J.; Waite, W.F.; Collett, T.S.; Kumar, P. 2D Micromodel Study of Clogging Behavior of Fine-Grained Particles Associated with Gas Hydrate Production in NGHP-02 Gas Hydrate Reservoir Sediments. *Mar. Pet. Geol.* **2019**, *108*, 714–730. [CrossRef]
32. Bigna, Y.; Oyeneyin, M.S.; Peden, J.M. Investigation of Pore-Blocking Mechanism in Gravel Packs in the Management and Control of Fines Migration. In Proceedings of the SPE Formation Damage Control Symposium, Lafayette, Louisiana, 7–10 February 1994; p. SPE-27342-MS.
33. Oyeneyin, B.; Peden, J.; Hosseini, A.; Ren, G. Factors to Consider in the Effective Management and Control of Fines Migration in High Permeability Sands. In Proceedings of the SPE European Formation Damage Conference, The Hague, The Netherlands, 15–16 May 1995. [CrossRef]
34. Khilar, K.C.; Fogler, H.S. *Migrations of Fines in Porous Media*; Springer Science & Business Media: Berlin/Heidelberg, Germany, 1998; Volume 12, ISBN 0-7923-5284-X.
35. Zhou, S.; Chen, W.; Li, Q.P.; Zhou, J.; Shi, H. CNOOC Research on the Solid Fluidization Well Testing and Production for Shallow Non-Diagenetic Natural Gas Hydrate in Deep Water Area. *China Offshore Oil Gas* **2017**, *29*, 1–8.
36. Lu, H.F.; Chen, H.; Chen, F.; Liao, Z.L. Mineralogy of the Sediments from Gas Hydrate Drilling Site, Shenhu Area, South China Sea. *Geol. Res. South China Sea* **2009**, *20*. (In Chinese with English Abstract).
37. Han, G.; Kwon, T.-H.; Lee, J.Y.; Jung, J. Fines Migration and Pore Clogging Induced by Single- and Two-Phase Fluid Flows in Porous Media: From the Perspectives of Particle Detachment and Particle-Level Forces. *Geomech. Energy Environ.* **2020**, *23*, 100131. [CrossRef]
38. White, F.M. *Fluid Mechanics*; The McGraw Hill Companies: New York, NY, USA, 2008; ISBN 0-07-352934-6.
39. Israelachvili, J. *Intermolecular and Surface Forces*; Academic Press: Cambridge, MA, USA, 1992; Volume 2.
40. Suzuki, S.; Kuwano, R. Evaluation on Stability of Sand Control in Mining Methane Hydrate. *Seisan Kenkyu* **2016**, *68*, 311–314.
41. Kwon, T.-H.; Lee, K.-R.; Cho, G.-C.; Lee, J.Y. Geotechnical Properties of Deep Oceanic Sediments Recovered from the Hydrate Occurrence Regions in the Ulleung Basin, East Sea, Offshore Korea. *Mar. Pet. Geol.* **2011**, *28*, 1870–1883. [CrossRef]
42. Winters, W.J.; Wilcox-Cline, R.W.; Long, P.; Dewri, S.K.; Kumar, P.; Stern, L.; Kerr, L. Comparison of the Physical and Geotechnical Properties of Gas-Hydrate-Bearing Sediments from Offshore India and Other Gas-Hydrate-Reservoir Systems. *Mar. Pet. Geol.* **2014**, *58*, 139–167. [CrossRef]
43. Egawa, K.; Nishimura, O.; Izumi, S.; Fukami, E.; Jin, Y.; Kida, M.; Konno, Y.; Yoneda, J.; Ito, T.; Suzuki, K.; et al. Bulk Sediment Mineralogy of Gas Hydrate Reservoir at the East Nankai Offshore Production Test Site. *Mar. Pet. Geol.* **2015**, *66*, 379–387. [CrossRef]